Polyelectrolyte domains in intrinsically disordered regions differentially regulate intracellular biomolecular condensation

Yoon Jeong Choi[1,2,3], Yujin Lee[1,6], Soojin Cho[1,6], Yaqi Pan [1,6], Changi Pack[4,5], Yemuk Kang[1], Youngtae Jeong[2,3], and Kiwon Song[1,*]

[1]Department of Biochemistry, College of Life Science and Biotechnology, Yonsei University, Seoul 03722, Republic of Korea

[2]Department of New Biology, DGIST, Daegu, 43014, Korea

[3]New Biology Research Center, DGIST, Daegu, 43014, Korea

[4]Department of Biomedical Engineering, University of Ulsan College of Medicine, Seoul 05505, South Korea

[5]Convergence Medicine Research Center, Asan Institute for Life Sciences, Asan Medical Center, Seoul 05505, South Korea

[6]These authors contributed equally.

*Correspondence: bc5012@yonsei.ac.kr

SUMMARY

Intracellular condensation is a hallmark of many proteins containing intrinsically disordered regions (IDRs). Decoding the regulatory mechanisms of condensation encoded within the amino acid sequences of condensate-forming proteins is essential for understanding both how intracellular condensates assemble and how they contribute to various disease pathologies. Here, we investigated the budding yeast P-body proteins Nst1 and Edc3, which exhibit pronounced intracellular self-condensation, and identified charged amino acid clusters in the low complexity regions (LCRs) that modulate their phase behavior. Guided by the stickers-and-spacers framework, we hypothesized that clusters of charged

residues within IDRs function in promoting intracellular condensation process. Using a sliding-window approach, we designated and dissected the polyelectrolyte (PE) domains of Nst1 and Edc3 and established their essential contributions to condensate coalescence. In Nst1, the polyanionic (PA) subdomain enhances intermolecular attraction and promotes coalescence, whereas the polyampholyte (PAM) subdomain imparts rigidity to the condensate as a distinct modulatory element and recruits additional components into the condensate. PA of Edc3 also regulates coalescence. Extending these findings to the neurodegenerative disease-associated protein TDP-43, we show that its PA regions are critical for coalescence, consistent with the presence of negatively charged amino acid clusters as potent molecular stickers functioning in condensate coalescence in cells. These results highlight charged-residue clusters as versatile sequence determinants of phase behavior and indicate that their systematic identification will be pivotal to defining the molecular grammar of protein condensation underlying the condensation of disease-related proteins.

KEYWORDS

biomolecular condensates, intrinsically disordered region (IDR), stickers and spacers model, polyelectrolyte, coalescence, polyampholyte, polyanion, P-body, Nst1, Edc3, TDP-43

INTRODUCTION

Biomolecular condensation observed in cells not only deepens our understanding of molecular dynamics in response to various physiological conditions, but also shed light on the mechanisms underlying protein amyloid formation (Alberti and Hyman, 2021; Alshareedah et al., 2024; Banani et al., 2017; Niu et al., 2023). These condensations occur within the crowded and complex cellular environment, exhibiting diverse physical properties depending on the degree of condensation.

Liquid-liquid phase separation (LLPS) represents one form of condensation, characterized by partitioned liquid-like droplets distinct from solidified protein amyloids (Ranganathan et al., 2022). Neurodegeneration-associated proteins usually act as scaffolds that drive the formation of liquid-like

condensates with self-condensation ability and high multivalency. Recent studies have increasingly reported the co-occurrence of amyloid fibrils and liquid-like condensates of pathogenic proteins, such as TDP-43, both in the brain tissues of patients with neurodegenerative diseases and in cellular models of these diseases (Ahmad et al., 2022; Alshareedah *et al.*, 2024; Gruijs da Silva et al., 2022; Sneideriene et al., 2025). This observation strongly suggests that the aggregation of pathogenic proteins does not proceed through direct solid aggregation, but rather through prior enrichment into liquid-like condensates, followed by a structural conversion into amyloid assemblies. That is, dysregulation of these liquid-like condensates is expected to promote the formation of protein amyloids implicated in neurodegenerative disorders (Hurtle et al., 2023; Nam and Gwon, 2023; Visser et al., 2024). Therefore, elucidating the underlying mechanisms of liquid-like condensation is critical both for understanding the molecular dynamics underlying physiological condensate formation, and for identifying therapeutic strategies to regulate pathological condensate formation (Alberti and Hyman, 2021; Choi et al., 2024; Gao et al., 2023; Lu et al., 2024; Mehta and Zhang, 2022).

Stickers-and-spacers model is a leading framework of a molecular mechanism for biomolecular liquid-like condensation (Banjade and Rosen, 2014; Choi et al., 2020; Sood and Zhang, 2024). This model defines “stickers” as molecular elements that mediate attractive interactions, and “spacers” as flexible linkers that separate stickers and modulate condensate properties (Choi *et al.*, 2020). Amino acids in intrinsically disordered regions (IDRs), capable of functioning as stickers, were precisely identified through *in vitro* studies. The cation-π interaction between tyrosine and arginine, as well as the interaction between lysine and RNA, were revealed to act as stickers (Ukmar-Godec et al., 2019; Wang et al., 2018b). The sequential pattern of these components significantly influences the dynamic characteristics of the condensate (Alshareedah *et al.*, 2024; Alshareedah et al., 2021; Wang *et al.*, 2018b). Notably, when sticker amino acids are clustered within the sequence, rather than dispersed, the resultant condensate tends towards solidification (Alshareedah *et al.*, 2024; Alshareedah *et al.*, 2021; Wang *et al.*, 2018b). Thus, the stickers-and-spacers model offers a solid basis for elucidating the condensation characteristics of molecules *in vitro*, offering valuable insights into the behavior of biomolecular condensates.

Despite the explanatory power of the stickers-and-spacers model, the molecular grammar underlying intracellular biomolecular condensation remains enigmatic. First, the morphology and physical properties

of condensates depend on the characteristics of condensate-forming proteins and the intracellular environment, and these properties can change over time as condensation progresses. In other words, the stickers that function may vary depending on the phase of condensation. Second, although the molecular grammar of condensation has been extensively characterized for prion-like low-complexity domains (PLCDs) - such as poly Q/N tracts in yeast amyloidogenic proteins and the RGG motifs in disease-related proteins like FUS and TDP-43 (Patel et al., 2015; Sanders et al., 2020; Wang et al., 2018), other intrinsically disordered regions (IDRs) with distinct combinations of sticker amino acids remain largely unexplored. Critically, many IDRs lack canonical PLCD features but still drive phase separation, suggesting the existence of alternative molecular grammars.

Recent *in vitro* and simulation studies have reported that the charge distribution within amino acid sequences strongly affects the viscosity, surface tension, and dynamic properties of condensates (Biswas and Potoyan, 2024; Linsenmeier et al., 2023; Sundaravadivelu Devarajan et al., 2024). These reports strongly indicate the need for research on the regulation of cellular condensation process by novel low complexity regions (LCRs) composed of sticker amino acids such as charged amino acid clusters, in addition to the previously studied PLCDs.

In this study, we aimed to elucidate the role of the polyelectrolyte region in the cellular condensation of biomolecules via Nst1. Both Nst1 and Edc3, established P-body components in budding yeast, possess intrinsic self-condensation capabilities. Upon Nst1 and Edc3 overexpression, cells initially exhibit numerous small puncta of Nst1 and Edc3, which progressively fuse into larger structures over time, thereby reducing the overall number of observed puncta (Fig. 1A). Utilizing this model, we examined how the polyelectrolyte region affects both the molecular dynamics of NST1 condensates and the condensate formation of P-body components mediated by NST1. Furthermore, we investigated whether the function of the polyelectrolyte region in Nst1 condensation could be extrapolated to TDP-43, a stress granule constituent that plays a pivotal role in stress granule dynamics and is closely linked to the pathology of neurodegenerative diseases.

RESULTS

Overexpression of Nst1 and Edc3 leads to mature condensate formation, whereas overexpression of their polyelectrolyte (PE) domain deletion mutants within the IDR maintains a stabilized microphase-separated state.

In our previous study, we reported that GFP-tagged Nst1 and Edc3, when overexpressed under the control of the GAL promoter, formed condensates that were larger and denser than those formed by Dcp2 or Dhh1 (Choi et al., 2022). Here, we monitored the formation dynamics of these condensates from the early phase of Nst1 and Edc3 overexpression until their intracellular expression levels reached saturation (Fig. 1A). Numerous small condensates—here referred to as microphase-separated structures—began to appear simultaneously throughout the cell as early as 1 hour after galactose induction and were observed in nearly all cells by 2 hours. When we analyze the mean integrated density and the number of puncta of each cell at 4 hours post-induction, the number of condensates per cell had decreased, while their internal density had increased markedly, indicative of a transition to a mature condensate state (Fig. 1B). These observations suggest that microphase Nst1 condensates progressively undergo coalescence as the intracellular concentration of Nst1 rises.

Next, we confirmed this distinctive self-condensation potential of Nst1 and Edc3 through analysis of puncta formation patterns in correlation with cytoplasmic protein concentration (Fig. 1C-D). Every molecule has its own critical concentration at which it forms a condensate, and a lower critical concentration indicates a higher potential for molecular condensation. By measuring the cytoplasmic concentration of proteins and correlating it with the degree of puncta formation (microphase separation, mature condensates), we can compare condensation patterns between proteins under cellular conditions. Using a galactose promoter, GFP-tagged P-body components such as Nst1, Edc3, Dcp2, and Dhh1, along with the stress granule component Pab1, were overexpressed for 4 hours. Afterward, the cytoplasmic concentration of the overexpressed proteins and the degree of self-condensation were measured using fluorescence correlation spectroscopy (FCS) (Fig.1 A, C-D). We classified the patterns of puncta formation into three categories: diffuse state, microphase separation, and mature condensates (Fig. 1A). GFP control did not exhibit puncta formation at any measured cytoplasmic concentration,

whereas Nst1 and Edc3 demonstrated mature condensates at remarkably low concentrations (Fig. 1C-D). Another P-body component, Dcp2 and Dhh1, exhibited microphase separation at higher cytoplasmic concentrations than the concentrations required for mature condensate formation by Nst1 and Edc3. However, mature condensates similar to those observed with Nst1 and Edc3 were not detected for Dcp2 and Dhh1 (Fig. 1C-D). These results confirm that, compared to Dcp2 and Dhh1, Nst1 and Edc3 have a greater intrinsic propensity for self-condensation in cells, which indicates their intrinsic potential for condensation.

Next, we hypothesized that a particular charged-amino acid cluster within intrinsically disordered regions (IDRs) in Nst1 protein sequence may function as a “sticker” domain during condensate formation. In our previous study, we identified that PD (polyampholyte domain), a segment of a charged-amino acid cluster in Nst1, functions in the condensation of other P-body components in cells overexpressing Nst1 (Choi *et al.*, 2022). However, Nst1 has extended charged amino acid regions beyond PD. We systematically searched for polyelectrolyte-like clusters of charged amino acids in the IDRs of Nst1 and Edc3 using a sliding window approach, as described in Supplementary Figure 1E (Fig. 1E). Charged amino acids (K, R, H, D, E) were classified, and their proportion within each window was calculated to generate a scoring system. Subsequently, a density plot of charged amino acids was created based on their positions within the sequence (Fig. 1E, S1, S2). Using this method, we segmented polyelectrolyte (PE) amino acid sequence regions spanning residues 65–205 in Edc3 and 460–752 in Nst1 (Fig. 1F, S1, S2).

Then, we generated deletion mutant clones of Nst1ΔPE and Edc3ΔPE, overexpressed each protein, and observed the cells after 4 hours of induction. Consistent with previous findings, overexpression of Nst1 deleted with the aggregation prone domain (APD), Nst1ΔAPD, did not result in condensate formation (Choi *et al.*, 2022) even at higher cytoplasmic concentrations (24 h induction), while those overexpressing wild-type Nst1 and Edc3 formed mature condensates (Fig. 1G-J). Interestingly, cells overexpressing the PE deletion mutants of both Nst1 and Edc3 exhibited microphase separation, even when their cytoplasmic concentrations were comparable with those of wild type Nst1 and Edc3 (Fig. 1G-J). To rule out insufficient expression or time as the cause of microphase separation, we extended the culture to 24 hours in galactose medium. However, even after prolonged induction, both Nst1ΔPE and

Edc3ΔPE failed to form mature condensates and continued to exhibit microphase separation (Fig. 1G, H). These results indicate that each polyelectrolyte (PE) is necessary for the coalescence of both Nst1 and Edc3 condensates, thereby facilitating the formation of mature condensates of Nst1 and Edc3.

Polyanion (PA) domain of the Polyelectrolyte (PE) region specifically promotes the coalescence of Nst1 condensates, whereas the polyampholyte (PAM) domain in the PE region does not.

Since the PE region of Nst1 exhibits a unique pattern of charged amino acid arrangement compared to the PE region of Edc3, the PE region of Nst1 was further characterized. Analysis of the Nst1 PE region using FELLS (http://protein.bio.unipd.it/fells/ BioComputing UP) revealed two distinct segments: a polyanion (PA) region spanning residues 460–631, a cluster consisting of remarkably high proportion of negatively charged amino acids, and a polyampholyte (PAM) domain spanning residues 632–752 (Fig. 2 A, B). In our previous study, we reported that the PAM domain (PD in the previous report) is required for promoting the condensation of other P-body components such as Dcp2 and Dhh1, which is induced by Nst1 condensation, but does not affect the self-condensation of Nst1 (Choi *et al.*, 2022).

To validate whether the effects of PE on Nst1 condensation were specifically due to the PA domain, we observed the time-dependent pattern of puncta formation of each GFP-tagged Nst1 domain deletion mutant in *Δnst1* cells. When overexpressed for 1 hour using the galactose induction system, the wild-type Nst1 (Nst1 full-length, F.L.), Nst1ΔPA, Nst1ΔPAM, and Nst1ΔPE all formed microphase separation (Fig. 2C). After 4 hours of induction, wild-type Nst1 and Nst1ΔPAM exhibited mature condensates with a reduced number of puncta per cell, indicating that the numerous small puncta observed after 1 hour of induction coalesced into fewer, larger puncta as the cytoplasmic concentration increased over time. (Fig. 2C). However, cells overexpressing Nst1ΔPA and Nst1ΔPE failed to undergo coalescence, and showed an increased number of puncta and decreased signal intensities compared to cells overexpressing wildtype Nst1 and Nst1ΔPAM (Fig. 2C). Even after 24 hours of induction, wild-type Nst1 and Nst1ΔPAM formed mature condensates with intense fluorescence signals (Fig. 2C). However, cells expressing Nst1ΔPA and Nst1ΔPE did not show a reduction in puncta number, although some puncta increased in

size and intensity compared to those observed after 4 hours of induction (Fig. 2C). This result indicates that PA domain is essential for coalescence of Nst1 condensates. Since several mutations in a protein can alter the physical property of condensates (Banani et al., 2022; Sanfeliu-Cerdan et al., 2023), we also determined whether these condensates exhibit LLPS or amyloid-like characteristics. Cells overexpressing each domain deletion mutant for 4 hours were treated with 1,6-hexanediol for 1 hour, then observed. Most puncta generated by each mutant dispersed upon treatment, indicating that none of the domains significantly alters the liquid-like properties of these condensates (Fig. 2D).

To evaluate the condensation potential of each domain deletion mutant, we measured the protein concentrations associated with each intracellular puncta formation pattern for each Nst1 variant after 4 hours of induction by FCS (Fig. 2E). Cells expressing GFP or Nst1ΔAPD remained diffuse, whereas cells expressing Nst1ΔPA or Nst1ΔPE exhibited microphase separation without forming mature condensates, despite having cytoplasmic protein concentrations comparable to those of wild-type Nst1 and Nst1ΔPAM (Fig. 2E).

When we initially constructed the Nst1ΔPA mutant, positively charged amino acids near the C-terminal portion of the defined PA region were included in the deletion. To better distinguish the function of negatively charged clusters within this region, we generated an additional mutant called Nst1ΔPA-1 that excluded positively charged amino acids from deletion while maintaining the integrity of the negatively-charged domain within PA. Consistently, cells overexpressing Nst1ΔPA-1 displayed numerous microphase separations from 1hour to 24 hours induction, similar to cells overexpressing Nst1ΔPA (Fig. S4). These findings indicate that the overexpression phenotype observed in Nst1ΔPA is due to the polyanion located within the PA region.

Next, we investigated whether the results from the Nst1 domain deletion mutants could be applied in condensate formation of endogenous Nst1. Since endogenously expressed Nst1 forms condensates from diauxic shift to stationary phase (Fig. 2F), we examined the puncta generation patterns by condensation of endogenously expressed full-length Nst1, the Nst1ΔPA, the Nst1ΔPAM, and the Nst1ΔAPD from early log phase to stationary phase (Fig. 2F).

We cultured cells expressing the chromosome-integrated GFP-tagged versions of each domain deletion mutant under the control of the endogenous Nst1 promoter in a *Δnst1* strain and observed them at 16, 30, 48, and 80 hours after seeding at an initial OD_{600} = 0.1 (Fig. 2G). These mutants exhibited similar puncta generation patterns to those observed in cells overexpressing these deletion mutants. Consistent with previous reports (Choi *et al.*, 2022), Nst1ΔAPD did not form puncta, confirming that the aggregation-prone region critical for hydrophobic core assembly is essential for condensate formation (Fig. 2H-I). Among the tested mutants, Nst1ΔPA was the first to initiate condensation, starting at 10 hours during the early log phase (Fig. 2H-I), and notably during the mid-log phase (14–18 hours). While the wild-type Nst1 and other mutants had not yet begun puncta formation, Nst1ΔPA condensates increased significantly (Fig. 2H-I). After 18 hours, condensation began for the full-length Nst1 and Nst1ΔPAM. Interestingly, starting at 22 hours, as cells entered the stationary phase, the intensity of Nst1ΔPAM condensates were markedly higher than those of the wild-type Nst1 and Nst1ΔPA condensates (Fig. 2I). At 46 hours, during the stationary phase, we observed that the intensities of Nst1ΔPA condensates were lower than those of wild-type Nst1 and Nst1ΔPAM condensates (Fig. 2J). Together, these findings demonstrate that each domain of IDR differentially contributes to Nst1 condensation even under physiological conditions.

Polyanion (PA) domain exclusively functions in coalescence of Nst1 condensates.

Next, we investigated whether the contribution of the PA domain to Nst1 condensation is unique to the PA region, or whether other sequence regions of similar size can also play a similar role, thereby assessing potential non-specific effects arising from deletions of comparable regions. To clarify this, we generated five additional domain deletion mutants of similar size as the PA domain in Nst1: Nst1ΔD1$^{2\text{-}122}$, Nst1ΔD2$^{123\text{-}293}$, Nst1ΔD3$^{294\text{-}459}$, Nst1ΔD4$^{753\text{-}844}$, Nst1ΔD5$^{845\text{-}1015}$ (Fig. 3A). The *Δnst1* w303a cells were transformed with plasmids that can overexpress each GFP-tagged Nst1 domain deletion mutant (D1~D5). All strains were induced with galactose and observed over time using a fluorescence microscope at specified time points after the induction (Fig. 3B).

Except the Nst1ΔAPD deletion mutant, the overexpression of D1~D5 deletion mutants began to induce condensates approximately 1 hour after galactose induction (Fig. 3B). Similar to the Nst1ΔPAM (Fig. 2C, 3B), the condensates of the deletion mutants from D1 to D5, increased in size as the number of condensates per cell decreased, except for the Nst1ΔPA (Fig. 3B). When cytoplasmic protein concentrations were measured by FCS after 4 hours of induction, Nst1ΔPA exhibited microphase separation at all measured concentrations, whereas all other mutants formed mature condensates at similar cytoplasmic concentrations (Fig. 3C). Even after 24 hours of induction, Nst1ΔPA failed to generate mature condensates, while all the other mutants, ΔD1 to ΔD5, successfully formed mature condensates (Fig. 3B). These results further support that the function of the negatively charged amino acid cluster in the IDR of Nst1 is unique and critical for coalescence of condensates in the process of biomolecular condensation of Nst1.

The polyanion (PA) domain of Nst1 enhances intermolecular interaction, whereas the polyampholyte (PAM) domain of Nst1 increases the rigidity of Nst1 condensates.

Next, we examined whether the PA and PAM domains influence the dynamics of Nst1 condensates by employing fluorescence recovery after photobleaching (FRAP). Since the condensates of the overexpressed Nst1ΔPA did not coalescence and retained minimal puncta size, the abnormal function in the coalescence process is likely related to the molecular dynamics affected by the PA domain deletion.

We examined GFP-tagged the full-length Nst1, as well as the Nst1ΔPA, Nst1ΔPAM, and Nst1ΔD1 mutants, with GFP control after 4 hours of induction (Fig. 4A). Puncta from each mutant were imaged, photobleached, and fluorescence recovery was monitored over time (Fig. 4B). Prior to be analyzed, recovery curves from each mutant FRAP analysis were fitted and normalized (Fig. 4C-D, S6 A-E). Because molecular dynamics can be affected by molecular size (Pack, 2021), the Nst1ΔD1 mutant was also used as a size control for the analyses of Nst1ΔPA and Nst1ΔPAM.

We measured the maximal recovery velocity and recovery half-life for each Nst1 domain deletion mutant (Fig. 4C, F-G). The maximal recovery velocity represents the rate at which unbleached fluorescent molecules exchange with bleached molecules within puncta; a lower maximal recovery velocity indicates stronger intermolecular interactions within condensates, while a higher velocity suggests weaker interactions and increased molecular dynamics. The recovery half-life reflects the time required for fluorescence in the bleached region to reach half of its maximum equilibrium intensity, serving as an additional measure of molecular dynamics. The full-length Nst1 exhibited the slowest and lowest maximal recovery velocity among all samples, whereas the PAM-, PA-, and D1-deleted mutants recovered more rapidly (Fig. 4D-F), indicating that molecules with smaller molecular weight are generally more dynamic in the condensates. Notably, Nst1ΔPA puncta showed the fastest maximal recovery velocity among all deletion mutants (Fig. 4F). In contrast, the maximal recovery velocity and half-life of Nst1ΔPAM were comparable to those of Nst1ΔD1 (Fig. 4F-G). These results suggest that Nst1ΔPA exhibits particularly increased molecular dynamics due to weaker and less stable intermolecular interactions compared to Nst1ΔPAM and Nst1ΔD1.

Regarding mobile fraction as area under curve (AUC, %), the full-length Nst1 had the lowest AUC compared with these Nst1 deletion mutant proteins (Fig. 4E). The AUC of the Nst1Δ PAM was significantly higher than those of the Nst1ΔPA and Nst1ΔD1 (Fig. 4H). This indicates that puncta formed by Nst1ΔPAM have a higher proportion of mobile fractions compared to those formed by Nst1ΔPA and Nst1ΔD1. This suggests that the PAM domain of Nst1 enhances the rigidity of Nst1 condensates.

Overall, our results strongly suggest that polyampholyte (PAM) deletion weakens cohesion of internal networks, increasing overall molecular mobility within the condensate, while the polyanion (PA) deletion specifically enhances single-molecule dynamics by reducing electrostatic molecular affinity. That is, polyanions might participate in intermolecular interactions, enforcing molecular affinity, while polyampholytes contribute to restricting the movement of molecules in the confined state within condensates. These results highlight how different charged domains contribute uniquely to condensate properties and molecular behavior.

The PAM domain is an RNA-independent multivalent interaction domain for interaction with a P-body component, Dcp2.

In our previous study, we found that overexpression of Nst1 induces the formation of Nst1 condensates, which simultaneously promote the condensation of other P-body components, including Dcp2 (Choi *et al.*, 2022). We suggested that the PAM domain, previously described as PD, is a multivalent interaction region responsible for the condensation of P-body components such as Dcp2 (Choi *et al.*, 2022).

Since the function of PAM domain was resolved by measuring endogenously expressing GFP-tagged Dcp2, Dhh1, and Xrn1 in cells overexpressing non-tagged Nst1 variants (Choi *et al.*, 2022), we need to confirm the function of PAM domain using a direct approach that can elucidate its role in inducing Dcp2 condensation. We utilized the chromosomally mKate2-tagged Dcp2 strain overexpressing GFP-tagged Nst1 variants, including Nst1ΔPAM, Nst1ΔPA, and Nst1ΔD1. The cells were induced to generate condensates of each Nst1 variant by 4 hour-overexpression, then treated with cycloheximide which binds to the ribosomal A site and inhibits translation elongation, resulting in decrease of free RNA level (Schneider-Poetsch et al., 2010). The reduction of the cytoplasmic concentration of free RNA, thereby eliminates Dcp2 condensates that are formed by free RNA (Teixeira et al., 2005; Van Treeck and Parker, 2018). With this strategy, the majority of Dcp2 condensates formed by Nst1 variants could be observed under these conditions (Fig. 5A).

Using high-resolution confocal microscopy, we clearly observed the formation of mixed or multiphasic condensates composed of Nst1 and Dcp2 (Fig. 5B). Most wild-type Nst1 condensates were co-localized with mKate2-tagged Dcp2, suggesting that Nst1 condensates promote the formation of Dcp2 condensates (Fig. 5C). Interestingly, the fluorescence signals from Nst1 and Dcp2 condensates did not completely overlap; instead, the two signals appeared as if distinct condensates were docked together (Fig. 5B).

To further investigate potential intermolecular interactions between Nst1 and Dcp2, we performed fluorescence cross-correlation spectroscopy (FCCS). However, no correlation between the two signals

was detected, indicating that individual Nst1 and Dcp2 molecules do not directly interact with each other (data not shown). These findings suggest that Dcp2 condensation induced by Nst1 overexpression is not mediated by direct intermolecular interactions but rather occurs as a consequence of the Nst1 condensation process itself.

Both Nst1ΔPA and Nst1ΔD1 condensates also exhibited co-localization with Dcp2-mKate2 condensates (Fig. 5B-C). Although Nst1ΔPA condensates were able to induce Dcp2 condensation, their size was relatively smaller compared to other Nst1 variant condensates, reminding the unique role of PA in coalescence of microphase condensates (Fig. 5B). In contrast, Nst1ΔPAM condensates rarely promoted the formation of Dcp2 condensates, highlighting the critical role of the PAM domain in facilitating Dcp2 condensation upon Nst1 overexpression (Fig. 5B-C).

These observations suggest that if the PAM domain induces Dcp2 condensation directly, rather than via RNA, then the number of Dcp2 condensates should not be reduced in Nst1ΔPA cells even after cycloheximide treatment, because Nst1ΔPA condensates, which contain the PAM domain, fail to coalesce and instead increase in number. In contrast, Nst1ΔPAM should lead to a significant reduction in the number of Dcp2 condensates (Fig. 5D). Condensates formed by overexpression of GFP-tagged Nst1 and its mutants demonstrated no change in the integrated density of puncta before and after CHX treatment (S7. A). This indicates that a decrease in cytoplasmic concentration of ribosomal free RNA induced by CHX treatment does not affect Nst1 condensation.

To further verify the role of PAM, we quantitatively measured Dcp2 condensation induced by overexpression of Nst1ΔPA and Nst1ΔPAM in each cell. For the quantitative analysis of Dcp2 condensates induced by condensation of wild-type Nst1 and its domain deletion mutants, instead of relying on the weak signals from mKate2-tagged Dcp2, we employed a GFP-tagged Dcp2 strain that allowed more robust quantification to further validate the function of the PAM domain (Fig. 5D). Cells overexpressing either non-tagged full-length Nst1 or the deletion mutants (Nst1ΔPA, Nst1ΔPAM) for 4 hours were treated with cycloheximide for 10 minutes prior to imaging. Subsequently, the puncta formed by chromosomally EGFP-tagged Dcp2 in these overexpression conditions were segmented and quantified (Fig. 5D-E). Notably, cells overexpressing Nst1ΔPA exhibited a substantially higher number of

Dcp2 puncta per cell compared to cells overexpressing wild-type Nst1 (Fig. 5E), suggesting that the increased number of Nst1ΔPA condensates containing the PAM domain may promote the formation of a greater number of Dcp2 condensates than wild-type Nst1. In contrast, the number of Dcp2 puncta per cell was reduced in Nst1ΔPAM-overexpressing cells relative to the wild-type (Fig. 5E), indicating that the PAM domain provides a physical platform necessary for efficient Dcp2 condensation. Collectively, these results demonstrate that the patterns of Dcp2 puncta formation differ between the PA and PAM deletion mutants, as depicted in Fig. 5D.

To further elucidate how the PA and PAM domains of Nst1 influence condensate formation in relation to free-RNA, we analyzed GFP-Dcp2, GFP-Edc3, and GFP-Nst1 condensates in lysates derived from stationary-phase cells endogenously expressing each of these GFP-tagged proteins (Fig. 5F). Observations were conducted both before and after the addition of an RNase inhibitor, which prevents RNA degradation and increases the concentration of pre-initiation RNA complexes (Fig. 5F). Previous studies have demonstrated that P-bodies extracted from Xrn1-deleted cells disassemble upon RNase treatment *in vitro* (Teixeira *et al.*, 2005), suggesting that RNA serves as a scaffold for P-body formation. Based on this, we hypothesized that the condensation of specific P-body components would either increase or decrease depending on their reliance on RNA as a scaffold. If the condensation of a particular P-body component requires pre-initiation complex RNA, its condensation is expected to be promoted when the concentration of pre-initiation complex RNA increases. Conversely, if condensation is independent of pre-initiation complex RNA, an increase in pre-initiation complex RNA concentration would either reduce condensation or leave it unaffected.

As previously reported, we observed that puncta of Dcp2, which lacks self-condensation potential, became intensified after RNase inhibitor treatment, supporting free RNA dependency in Dcp2 condensate formation (Fig. 5G-H, and(Cohen et al., 2005; Tibble et al., 2021; Van Treeck and Parker, 2018). In contrast, we observed that Edc3 condensates decreased upon RNase inhibitor treatment (Fig. 5G-H). Since both Edc3 and pre-initiation complex RNA can function as scaffolds for P-body generation, this observation likely reflects the competition between Edc3 and RNA for inducing condensation.

To investigate the role of RNA in condensate formation mediated by Nst1 and its domains, we analyzed the puncta of endogenously expressed GFP-Nst1, GFP-Nst1ΔPA, and GFP-Nst1ΔPAM in stationary-phase cells, with or without RNase inhibitor treatment. Similar to Edc3, Nst1 condensates were reduced in cells treated with the RNase inhibitor (Fig. 5I-J). The condensates formed by the Nst1 ΔPA mutant displayed comparable intensity regardless of RNase inhibitor treatment (Fig. 5I-J). In contrast, the Nst1 ΔPAM mutant exhibited a significant increase in condensate intensity following RNase inhibitor treatment, suggesting an enhanced dependency of Nst1ΔPAM on pre-initiation RNA complexes (Fig. 5I-J). These findings strongly support that self-condensation of both Nst1 and Edc3 occurs independently of pre-initiation RNA complexes. Furthermore, the PAM domain appears to serve as an interaction platform that promotes RNA-independent condensation of other P-body components.

The Polyanion (PA) domain of human TDP-43 promotes coalescence of condensates, similar to Nst1.

We expanded the functional analysis of PA and PAM subdomains to the scaffold protein Edc3 focusing on their roles in biomolecular condensation. Since Edc3 also has a distinctive negative charged amino acid cluster in PE domain, we divided the PE domain of Edc3 into two parts: the PA region, characterized by a cluster of negatively charged amino acids, and the PAM region, where positively and negatively charged amino acids are more evenly distributed (Fig. S2, S8). We constructed plasmids for the overexpression of GFP-tagged Edc3ΔPAM and Edc3ΔPA mutants, and overexpressed them together with GFP-tagged Edc3, Edc3ΔPE, and Edc3ΔAPD in the *Δedc3* strain to examine their condensate phenotypes. Remarkably, as observed with Nst1, after 4 hours of overexpression, Edc3 formed mature condensates, whereas Edc3ΔPA, similar to Edc3ΔPE, exhibited microphase separation in all cells (Fig. S8). Even after 24 hours of induction, Edc3ΔPA failed to form mature condensates in almost all cells, and only microphase-separated condensates were observed, demonstrating the role of PA in coalescence of Edc3 condensates. Edc3ΔAPD, consistent with the result of Nst1, did not form condensates (Fig. S8).

We then investigated whether the phenotype of PA deletion mutants observed in the budding yeast proteins Nst1 and Edc3 is also present in proteins with self-condensation potential that are implicated in neurodegenerative diseases. Since TDP-43 are known to undergo self-condensation upon overexpression in budding yeast (Fushimi et al., 2011; Johnson et al., 2008; Outeiro and Lindquist, 2003; Sun et al., 2011), we first confirmed TDP-43 aggregation upon overexpression in budding yeast as been previously reported. Under the same overexpression conditions used for Nst1 and Edc3, TDP-43 also underwent self-condensation in budding yeast (Fig. 6B). Two PA domains (PA1, PA2) in the TDP-43 sequence were designated with using the sliding window approach (Fig. 6A, S3). The low complexity region in the C-terminal domain (CTD) has been known to be critical for TDP-43 amyloid aggregation (Chien et al., 2021; Li et al., 2021; Shenoy et al., 2023). The CTD has a relatively low charged amino acid cluster score, but within the CTD, residues 255-276, which have a relatively high density of charged amino acid, were designated as the PAM domain. To identify intrinsic sequence determinants of TDP-43 aggregation, we generated and overexpressed those deletion mutants of TDP-43 in the budding yeast system and monitored them over time. Strikingly, the PA1 and PA2 deletion mutants failed to form mature condensates at 4 hours of overexpression compared to the full-length TDP-43, suggesting their roles in coalescence of condensates as observed role of PA in Nst1 and Edc3 (Fig. 6B). Notably, the previously characterized CTD deletion mutant also formed condensates when overexpressed, similar to the reported study (Johnson *et al.*, 2008; Wang et al., 2018a). The morphology of these condensates differed from that of the full-length TDP-43: while the full-length TDP-43 formed both large and small, irregularly shaped condensates, the CTD deletion mutant produced very large, round condensates in much lower numbers per cell (Fig. 6B). Interestingly, the condensate morphology of the TDP-43ΔCTD mutant was recapitulated in the TDP-43ΔPAM mutant, suggesting that the phenotype might be attributable to the loss of the PAM domain within the CTD rather than the entire NTD existence or CTD deletion. This implies that the charged amino acid cluster within the CTD may play a key role in determining the physical properties and dynamics of TDP-43 condensates. Since these TDP-43 mutants generated retain the nuclear localization signal (NLS), all overexpressed mutants predominantly localize to and form condensates in the nucleus. To observe the condensates of mutants in the cytoplasm, we additionally generated NLS-mutated TDP-43 variants. These variants exhibited phenotypes similar to those observed in the nucleus,

except for the CTD-deleted TDP-43 variant: the PA1 and PA2 deletion mutants failed to form mature condensates (Fig 6B). Notably, while overexpressed TDP-43ΔCTD forms condensates in the nucleus, it remains diffusely distributed in the cytoplasm (Fig. 6B). The phenotypic pattern observed for each mutant after 4 hours of induction remained unchanged in cells induced for 8, 10, or 12 hours (S9).

We next investigated whether the TDP-43 coalescence tendency observed for the PA1 and PA2 mutants, when expressed in yeast, was attributable to the negative charges of the clustered amino acids. To this end, we generated *PA1-1*, *PA1-2*, *PA2-1*, and *PA2-2* mutants in which the glutamate (E) and aspartate (D) residues in the partial N- and C-terminal regions of PA1 and PA2 were individually substituted with glutamine (Q) and asparagine (N), respectively, as well as *PA1-1PA1-2* and *PA2-1PA2-2* mutants in which all glutamate and aspartate residues were replaced with glutamine and asparagine (Fig. 6C).

Strikingly, upon galactose induction in cells, the PA1 and PA2 mutants with all negatively charged amino acids replaced by uncharged glutamine and asparagine exhibited completely different profile in puncta formation of the wildtype TDP-43 protein (Fig. 6D). Unlike the ΔPA1 mutant, the *PA1-1PA1-2* mutant exhibited a distinct phenotype: while the overexpressed ΔPA1 mutant displayed microphase separation, the overexpressed *PA1-1PA1-2* showed a pronounced inhibition of condensation itself (Fig. 6D). This mutation appears to confer a gain of function, since substituting the negatively charged aspartic acid (D) and glutamic acid (E) residues in PA1 with uncharged but chemically similar glutamine (Q) and asparagine (N) not only abolishes coalescence, but also impairs the initial seeding of puncta formation—a property not observed in either the wild-type protein or the ΔPA1 mutant. Furthermore, the *PA1-1* mutant, with partial N-terminal substitution, exhibited morphology identical to wildtype condensates, whereas *PA1-2* resembled the *PA1-1PA1-2* mutant, suggesting that the substitution of E and D residues with Q and N within the ^{13}DEPIEIPSEDD^{23} region of PA1 is critical in driving this diffused phenotype. These results indicate that the gain of function induced by the specific substitutions in PA1 includes both the inhibition of coalescence and the blocking of seeding during puncta formation.

Notably, the results for PA2 domain are remarkable. The *PA2-1PA2-2* exhibited puncta morphology identical to that of ΔPA2 and, unlike the wildtype TDP-43, displayed a pronounced tendency toward

microphase separation (Fig. 6D). Unlike the PA1 mutants, both *PA2-1, PA2-2* mutant having partial substitution of negatively charged amino acids in either the N-terminal or C-terminal regions failed to fully recapitulate the puncta generation patterns of ΔPA2 (Fig. 6D). These results indicate that it is not specific negatively charged residues within PA2 that are critical, but rather the overall clusters of negative charged amino acids in PA2 contribute to TDP-43 coalescence.

To determine whether the condensate phenotypes of PA1, PA2, PAM, and CTD deletion mutants of TDP-43 observed in budding yeast are also present in mammalian cells, we overexpressed GFP-fused TDP-43 and TDP-43 mutants in U2OS cells. Consistent with our findings in budding yeast, the PA1 and PA2 deletion mutants did not form mature condensates in mammalian cells (Fig. 6E). In particular, the PA2 deletion mutant failed to form condensates in all cells expressing the protein, as indicated by the presence of GFP signal (Fig. 6E). Interestingly, the PAM domain deletion mutant exhibited a markedly larger size and stronger intensity of puncta formation compared to other mutants. To observe the condensation of TDP-43 derivatives in the cytoplasm, we introduced an additional ΔNLS (K82A, R83A, K84A) mutation into each TDP-43 domain deletion mutant and examined their expression in U2OS cells (Lu et al., 2022). The TDP-43 derivatives in the nucleus displayed a similar pattern of puncta formation. Notably, in the case of the ΔPA1ΔPA2 double deletion, puncta formation was further inhibited. These data suggest that PA domains could be a general key contributor to condensation of TDP-43.

DISCUSSION

Condensates by LLPS are known to undergo formation, maturation, and subsequent transition into aggregates within the cellular environment (Shen et al., 2023; Wang et al., 2021). Through *in vitro* studies, it has been found that the maturation of liquid-like condensates proceeds via three major principal mechanisms: coalescence, whereby individual condensates fuse to form larger structures; Ostwald ripening, in which constituent molecules from smaller condensates are transferred to larger ones, resulting in the growth of the latter and shrinkage of the former; and diffusion-limited growth, characterized by the incorporation of freely diffusing molecules into existing condensates (Banerjee et al., 2024; Lee et al., 2021; Linsenmeier et al., 2021). The intrinsic sequence properties of proteins are

believed to play critical roles in regulating each of these processes; however, *in vivo* studies elucidating their molecular grammar remain relatively limited.

Low complexity regions (LCRs) are particularly intriguing segments within protein sequences. They are composed of highly repetitive stretches consisting of just one or a few types of amino acids. It is known that, compared to prokaryotes, LCRs are more than 200 times more prevalent in eukaryotes (Dickson and Golding, 2022; Sim and Creamer, 2002). LCRs are closely associated with phenotypic variation (Fondon and Garner, 2004) and function as multivalent interaction hubs, playing a critical role in protein condensation and amyloidogenesis (Banjade and Rosen, 2014; Linsenmeier *et al.*, 2023). Collectively, these findings strongly suggest that LCRs are physiologically and pathologically important components in complex biological systems.

Charged amino acid clusters which is included in LCRs represent one of the most frequently observed sequence motifs within proteins consisting of RNP granules (Niedner-Boblenz et al., 2024; Regy et al., 2020; Saitoh et al., 2004). Within intrinsically disordered regions (IDRs), there have been numerous clues that certain charged amino acids may contribute to the regulation of condensation, either by promoting or inhibiting condensation (Saar et al., 2021). Both negative and positive charged amino acids are thought to modulate intermolecular affinity via electrostatic interactions, where the pattern of charged residues along the sequence plays a pivotal role. As mentioned previously, when charged residues are uniformly distributed, the driving force for phase separation is attenuated; in contrast, when charged residues are clustered or segregated from other residues, the propensity for phase separation is enhanced (Borcherds et al., 2021; Chen et al., 2021; Miyagi et al., 2022). Therefore, the charged amino acid clusters within condensate-forming proteins likely play critical roles in condensation.

This study presents the first report on the role of the low-complexity domains (LCDs) consisting of the negative charged amino acids, as sequence elements required for the maturation of protein condensates in cells. Deletion of the PA region in Nst1, Edc3, and TDP-43 allowed condensate formation but impaired their coalescence and maturation, suggesting that the PA domain may be generally required for the formation of mature condensates in other proteins as well.

Substituting the negatively charged aspartate (D) and glutamate (E) in the PA1 of TDP-43 with uncharged but chemically similar glutamine (Q) and asparagine (N) abolishes puncta formation or maturation, demonstrating the critical role of the negative charge cluster in PA1 for condensate seeding and coalescence (Fig. 6). This strongly suggests that the polyanion region plays a critical role in proteins with high condensation potential and underscores the necessity to further validate its function in TDP-43 condensation within mammalian models. Notably, in motor neurons of ALS-FTD patients, the reduction of intracellular TDP-43 monomer concentration due to aberrant condensation and aggregation is a major driver of disease progression (Kellett et al., 2025; Oiwa et al., 2023). Therefore, identifying domains capable of modulating TDP-43 condensation could represent an initial step toward developing novel therapeutic strategies. The PA1 and PA2 domains of TDP-43 identified in this study are short regions, each comprising approximately 20 amino acids. Subsequent studies should focus on pinpointing specific residues within PA1 and PA2 which function in TDP-43 coalescence.

Bioinformatics studies revealed that D/E repeats are widespread across eukaryotic proteomes (Wang et al., 2023), with nearly half of the proteins containing these negatively charged clusters being DNA/RNA-binding proteins (Wang *et al.*, 2023). In DNA-binding transcription factors such as HMGB1, RFX1, Sox11, and UBF1, these negative charge clusters are thought to interact with their own positive-charged DNA binding domains, mediating autoinhibition and thereby modulating DNA binding affinity. The recent research on HMGB1 is particularly noteworthy (Mensah et al., 2023). HMGB1 functions as a chromatin-binding architectural protein that regulates DNA accessibility, gene expression, and genome stability within the cell (Lange and Vasquez, 2009). The C-terminal domain of HMGB1, which consists of a negative charge amino acid cluster, when replaced by positively charged amino acids in a mutant, exhibits amorphous and rigid physical properties *in vitro*, contrasting with the wild-type protein. In addition, its mutants in which the negative charge amino acid cluster is deleted, fail to localize properly in the nucleolus, thereby influencing physiological function of HMGB1 (Mensah *et al.*, 2023). This suggests that a broader study is warranted on the correlation between the condensation behavior of proteins containing sequence-specific charged amino acid clusters and the effect of such condensation on their physiological functions.

Another noteworthy observation regarding the PAM domain deletion mutant of TDP-43 is that condensates formed by this mutant become enlarged compared to the condensates of wild-type (Fig. 6). A similar, though less pronounced, trend was also observed in Nst1 (Fig. 2). It is possible that deletion of the PAM domain reduces the local charge surrounding the PA domain, thereby amplifying the functional contribution of the PA domain. Furthermore, because loss of the PAM domain itself increases the fluidity of condensates, the combined effect of enhanced affinity and elevated fluidity may lead to the observed enlargement of condensates.

Altogether, our study provides compelling evidence that the arrangement of low complexity regions (LCRs) and clustered charged amino acids within proteins serves as a key regulator in the formation and maturation of biomolecular condensates associated with liquid-liquid phase separation (LLPS) in cell. These findings underscore the significance of correlating the patterns and organization of LCRs, such as charged clusters, with the material state, subcellular localization, and functional outcomes of condensates. Further investigation into the biochemical characteristics of condensates, which vary according to the molecular grammar of proteins, will illuminate the diverse physiological functions of condensates within cells, and may reveal a link between excessive condensate or aggregate formation and the onset of pathological states.

STAR★METHODS

KEY RESOURCES TABLE

REAGENT OR RESOURCE	SOURCE	IDENTIFIER
Antibodies		
goat anti-GFP	ROCKLAND, USA	Cat# 600-101-215
mouse anti-Tub1	Sigma, USA	Cat# T5168
anti-goat (secondary antibody)	Jackson ImmunoResearch Laboratories, Inc, USA	Cat# 705-035-003

anti-Mouse (secondary antibody)	Santa Cruz Biotechnology, USA	Cat# sc-2005
Bacterial and virus strains		
Escherichia coli DH5α cells One Shot™ TOP10 Chemically Competent *E. coli*	Invitrogen, USA	Cat# C404003
Biological samples		
Salmon sperm DNA (Deoxyribonucleic acid sodium salt from salmon testes)	Sigma, USA	Cat# D1626
Chemicals, peptides, and recombinant proteins		
1,6-Hexanediol	DAEJUNG CHEMICAL & METALS CO., LTD, South Korea	Cat# 629-11-8
4% paraformaldehyde	T&I, South Korea	Cat# BPP-9004
	Cytiva,USA,	Cat# SH30088.03
WestGlowTM PICO PLUS Chemiluminescent Substrate	BIOMAX, South Korea	Cat# BWP0200
20X TBS-T (20X Tris-Buffered Saline/1% Tween-20)	T&I, South Korea	Cat# BTT-9120
Antibiotic-antimycotic solution (Anti-Anti)	Gibco, USA,	Cat# 15240-062
Experimental models: Cell lines		
U2OS cells Human osteosarcoma cell line	ATCC	HTB-96
Experimental models: Organisms/strains		
Saccharomyces cerevisiae W303a *leu2-3,112 trp1-1 can1-100 ura3-1 ade2-1 his3-11,15*	S. Elledge	YSK3549
Saccharomyces cerevisiae W303a except as *Δedc3::KANMX*	this study	YSK3707
Saccharomyces cerevisiae W303a except as *Δnst1::KANMX*	this study	YSK3490
Saccharomyces cerevisiae W303a except as *NST1-EGFP::KANMX*	K.Song	YSK3498
Saccharomyces cerevisiae W303a except as *DCP2-EGFP::HIS3MX6*	K.Song	YSK3527
Saccharomyces cerevisiae W303a except as *EDC3-EGFP::HIS3MX6*	K.Song	YSK3528

Saccharomyces cerevisiae W303a except as *Δnst1::KANMX pNST1-GFP-NST1::URA3*	this study	YSK3700
Saccharomyces cerevisiae W303a except as *Δnst1::KANMX pNST1-GFP-NST1ΔPA::URA3*	this study	YSK3701
Saccharomyces cerevisiae W303a except as *Δnst1::KANMX pNST1-GFP-NST1ΔPAM::URA3*	this study	YSK3702
Saccharomyces cerevisiae W303a except as *Δnst1::KANMX pNST1-GFP-NST1ΔAPD::URA3*	this study	YSK3714
Saccharomyces cerevisiae W303a except as *Δnst1::KANMX PAB1-EGFP::HIS3MX6*	this study	YSK3704
Saccharomyces cerevisiae W303a expect as *Δnst1::KANMX EDC3-EGFP::HIS3MX6*	this study	YSK3694
Saccharomyces cerevisiae W303a expect as *Δnst1::KANMX DHH1-EGFP::HIS3MX6*	this study	YSK3695
Saccharomyces cerevisiae W303a expect as *Δnst1::KANMX DCP2-EGFP::HIS3MX6*	this study	YSK3709
Saccharomyces cerevisiae BY4741expect as *Δnst1::KANMX DCP2-mKate2-sphis5*	this study	YSK3663
Oligonucleotides		
pMW20(U)-pGAL-GFP-NST1Δ2-122 deletion top 5’ ATTACACATGGCATGGATGAACGAGCTCAGTTTAATGTCATAAGGAATTACC AGGACGAT 3’	this study	KS2262
pMW20(U)-pGAL-GFP-NST1Δ2-122 deletion bottom 5’ ATCGTCCTGGTAATTCCTTATGACATTAAACTGAGCTCGTTCATCCATGCCA TGTGTAAT 3’	this study	KS2263
pMW20(U)-pGAL-GFP-NST1Δ123-293 deletion top 5’ ACTATTCTACGAATCGAAAAGGAGGAAGTACAAAAAATGATGATGTATCCGA ATATTAGA 3’	this study	KS2384
pMW20(U)-pGAL-GFP-NST1Δ123-293 deletion bottom 5’ TCTAATATTCGGATACATCATCATTTTTTGTACTTCCTCCTTTTCGATTCGTA GAATAGT 3’	this study	KS2385

pMW20(U)-pGAL-GFP-NST1Δ294-459 deletion top 5' TCACATCCCAAAATAGCAGAGGAGTATGTAGAAGATGAAGATGAGGAAGAC TATGATGAC 3'	this study	KS2386
pMW20(U)-pGAL-GFP-NST1Δ294-459 deletion bottom 5' GTCATCATAGTCTTCCTCATCTTCATCTTCTACATACTCCTCTGCTATTTTGG GATGTGA 3'	this study	KS2387
pMW20(U)-pGAL-GFP-NST1Δ460-630 deletion top 5' GATACTTCGTTAGATACTGATTCTATATATCTAGAAGAAGAAAAAAGAAAGAA AAGAGAG 3'	this study	KS2280
pMW20(U)-pGAL-GFP-NST1Δ460-630 deletion bottom 5' CTCTCTTTTCTTTCTTTTTTCTTCTTCTAGATATATAGAATCAGTATCTAACGA AGTATC 3'	this study	KS2281
pMW20(U)-pGAL-GFP-NST1Δ755-844 deletion top 5' AGAGAACAGAAAAGGCTAGAACAAGAAAAGGATCTACTTCTTCCTTCAACTA ACAACCAG 3'	this study	KS2397
pMW20(U)-pGAL-GFP-NST1Δ755-844 deletion bottom 5' CTGGTTGTTAGTTGAAGGAAGAAGTAGATCCTTTTCTTGTTCTAGCCTTTTCT GTTCTCT 3'	this study	KS2398
pMW20(U)-pGAL-GFP-NST1Δ845-1015 deletion top 5' CCAGTTTCACCCACAGGCTTTAACGTTCATGATCAAAAAAGCTCATTTTCGG GACCGTCG 3'	this study	KS2388
pMW20(U)-pGAL-GFP-NST1Δ845-1015 deletion bottom 5' CGACGGTCCCGAAAATGAGCTTTTTTGATCATGAACGTTAAAGCCTGTGGG TGAAACTGG 3'	this study	KS2389
pMW20(U)-pGAL-GFP-NST1Δ460-596 deletion top 5' GATACTTCGTTAGATACTGATTCTATATATCGGAAATTGATTCAGATAGCCAT TACAAAG 3'	this study	KS2437
pMW20(U)-pGAL-GFP-NST1Δ460-596 deletion bottom 5'GATACTTCGTTAGATACTGATTCTATATATCGGAAATTGATTCAGATAGCC ATTACAAAG 3'	this study	KS2438
pMW20(U)-pGAL-GFP-EDC3Δ65-205 deletion top 5' AGGTTCTAACTGTTGCCTCTCCCAAATACCTACCAATAAC 3'	this study	KS2360

pMW20(U)-pGAL-GFP-EDC3Δ65-205 deletion bottom 5' GTTATTGGTAGGTATTTGGGAGAGGCAACAGTTAGAACCT 3'	this study	KS2361
pMW20(U)-pGAL-GFP-EDC3Δ65-180 deletion top 5' AAGGACTTAAAGGTTCTAACTGTTGCCTCTCCGCAACAAGATGCTCAAGATG ATCTGGTT 3'	this study	KS2446
pMW20(U)-pGAL-GFP-EDC3Δ65-180 deletion bottom 5' AACCAGATCATCTTGAGCATCTTGTTGCGGAGAGGCAACAGTTAGAACCTTT AAGTCCTT 3'	this study	KS2447
pMW20(U)-pGAL-GFP-EDC3Δ181-205 deletion top 5' AGAAATGAGCAAAGCACACACCAATCTCAGCCCAAATACCTACCAATAACTC AGTCTTTG 3'	this study	KS2444
pMW20(U)-pGAL-GFP-EDC3Δ181-205 deletion bottom 5' CAAAGACTGAGTTATTGGTAGGTATTTGGGCTGAGATTGGTGTGTGCTTTG CTCATTTCT 3'	this study	KS2445
pMW20(U)-pGAL-GFP-EDC3Δ330-380 deletion top 5' AACTAGGTGGCCGTGCACGTCTACAGGATTCCATGGTCAA 3'	this study	KS2362
pMW20(U)-pGAL-GFP-EDC3Δ330-380 deletion bottom 5' TTGACCATGGAATCCTGTAGACGTGCACGGCCACCTAGTT 3'	this study	KS2363
pMW20(U)-pGAL-GFP-TARDBP infusion cloning top 5' GCATGGATGAACGAGCTTCTGAATATATTCGGGTAAC 3'	this study	KS2401
pMW20(U)-pGAL-GFP-TARDBP infusion cloning bottom 5' GTCGACTCTAGAGGATCCCTACATTCCCCAGCCAGAAG 3'	this study	KS2402
pMW20(U)-pGAL-GFP-TARDBPΔ2-29 deletion top 5' GGGATTACACATGGCATGGATGAACGAGCTACGGTTACAGCCCAGTTTCCA GGGGCGTGT 3'	this study	KS2429
pMW20(U)-pGAL-GFP-TARDBPΔ2-29 deletion bottom 5' ACACGCCCCTGGAAACTGGGCTGTAACCGTAGCTCGTTCATCCATGCCATG TGTAATCCC 3'	this study	KS2430
pMW20(U)-pGAL-GFP-TARDBPΔ197-220 deletion top 5' CCTTTGAGAAGCAGAAAAGTGTTTGTGGGGTTCATCCCCAAGCCATTCAGG GCCTTTGCC 3'	this study	KS2448

pMW20(U)-pGAL-GFP-TARDBPΔ197-220 deletion bottom 5' GGCAAAGGCCCTGAATGGCTTGGGGATGAACCCCACAAACACTTTTCTGCTTCTCAAAGG 3'	this study	KS2449
pMW20(U)-pGAL-GFP-TARDBPΔ255-276 deletion top 5' GGAGAGGACTTGATCATTAAAGGAATCAGCGGTGGTAATCCAGGTGGCTTTGGGAATCAG 3'	this study	KS2431
pMW20(U)-pGAL-GFP-TARDBPΔ255-276 deletion bottom 5' CTGATTCCCAAAGCCACCTGGATTACCACCGCTGATTCCTTTAATGATCAAGTCCTCTCC 3'	this study	KS2432
pMW20(U)-pGAL-GFP-TARDBPΔ255-414 deletion top 5' GGACTTGATCATTAAAGGAATCAGCTAGGGATCCTCTAGAGTCGACCTGC 3'	this study	KS2439
pMW20(U)-pGAL-GFP-TARDBPΔ255-414 deletion bottom 5' GCAGGTCGACTCTAGAGGATCCCTAGCTGATTCCTTTAATGATCAAGTCC 3'	this study	KS2440
TARDBPΔNLS (K82A, R83A, K84A) top 5' GTGTATGTTGTCAACTATCCAAAAGATAACGCAGCAGCAATGGATGAGACAGATGCTTCATCAGCAGTG 3'	this study	KS2472
TARDBPΔNLS (K82A, R83A, K84A) bottom 5' CACTGCTGATGAAGCATCTGTCTCATCCATTGCTGCTGCGTTATCTTTTGGATAGTTGACAACATACAC 3'	this study	KS2473
pRS306-pNST1-GFP-NST1 infusion cloning top 5' CGTCCCGGGATGAGTAAAGGAGAAGAACTTTTC 3'	this study	KS2238
pRS306-pNST1-GFP-NST1 infusion cloning bottom 5' CGTCTCGAGCAAATTTAAGACGTTTGCGTAG 3'	this study	KS2239
pRS306-pNST1-GFP-NST1Δ460-630 top 5' GATACTTCGTTAGATACTGATTCTATATATCTAGAAGAAGAAAAAAGAAAGAAAAGAGAG 3'	this study	Ks2280
pRS306-pNST1-GFP-NST1Δ460-630 bottom 5' CTCTCTTTTCTTTCTTTTTTCTTCTTCTAGATATATAGAATCAGTATCTAACGAAGTATC 3'	this study	Ks2281

pRS306-pNST1-GFP-NST1Δ631-752 top 5' GATAATAACAGACTAAAACTTCTACAAGAACTACAGAAAGAAAAAGAAGAAG AAGAGAGA 3'	this study	KS2176
pRS306-pNST1-GFP-NST1Δ631-752 bottom 5' TCTCTCTTCTTCTTCTTTTTCTTTCTGTAGTTCTTGTAGAAGTTTTAGTCTGTT ATTATC 3'	this study	KS2177
pRS306-pNST1-GFP-NST1Δ1016-1240 top 5' GGCATGGATGAACGAGCTCAGGATCAAAAAAGCTCATTTTCG 3'	this study	KS2194
pRS306-pNST1-GFP-NST1Δ1016-1240 bottom 5' CGAAAATGAGCTTTTTTGATCCTGAGCTCGTTCATCCATGCC 3'	this study	KS2195
pcDNA3.1myc-HisA-GFP-TARDBP infusion cloning top 5'AGCTGGCTAGTTAAGCTTGGTACCATGAGTAAAGGAGAAGAACTTTTC 3'	this study	KS2455
pcDNA3.1myc-HisA-GFP-TARDBP infusion cloning bottom 5'GCGGCCGCCACTGTGCTGGATATCCTACATTCCCCAGCCAGAAGACTT 3'	this study	KS2456
TARDBP *PA1-1* (E3Q, E9Q, D10N, E11Q) ΔNLS (K82A, R83A, K84A) top 5' GCATGGATGAACGAGCTTCTCAGTATATTCGGGTAACCCAGAACCAGAACG ATGAGCCCATTGAAAT 3'	this study	KS2492
TARDBP *PA1-1* (E3Q, E9Q, D10N, E11Q) ΔNLS (K82A, R83A, K84A) bottom 5' ATTTCAATGGGCTCATCGTTCTGGTTCTGGGTTACCCGAATATACTGAGAAG CTCGTTCATCCATGC 3'	this study	KS2493
TARDBP *PA1-2* (D13N, E14Q, E17Q, E21Q, D22N, D23N) ΔNLS (K82A, R83A, K84A) top 5' GGGTAACCGAAGATGAGAACAACCAGCCCATTCAGATACCATCGCAGAACA ACGGGACGGTGCTGCTCTCCAC 3'	this study	KS2494
TARDBP *PA1-2* (D13N, E14Q, E17Q, E21Q, D22N, D23N) ΔNLS (K82A, R83A, K84A) bottom 5' GTGGAGAGCAGCACCGTCCCGTTGTTCTGCGATGGTATCTGAATGGGCTG GTTGTTCTCATCTTCGGTTACCC 3'	this study	KS2495
TARDBP *PA1-1PA1-2* (E3Q, E9Q, D10N, E11Q, D13N, E14Q, E17Q, E21Q, D22N, D23N) ΔNLS (K82A, R83A, K84A) top 5' GCATGGATGAACGAGCTTCTCAGTATATTCGGGTAACCCAGAACCAGAACA ACCAGCCCATTCAGAT 3'	this study	KS2500
TARDBP *PA1-1PA1-2* (E3Q, E9Q, D10N, E11Q, D13N, E14Q, E17Q, E21Q, D22N, D23N) ΔNLS (K82A, R83A, K84A) bottom 5' ATCTGAATGGGCTGGTTGTTCTGGTTCTGGGTTACCCGAATATACTGAGAA GCTCGTTCATCCATGC 3'	this study	KS2501

TARDBP *PA2-1* (E200Q, D201N, E204Q, D205N, E206Q, E209Q) ΔNLS (K82A, R83A, K84A) top 5' TGTTTGTGGGGCGCTGTACACAGAACATGACTCAGAACCAGCTGCGGCAGTTCTTCTCTCAGTACGGGGA 3'	this study	KS2484
TARDBP *PA2-1* (E200Q, D201N, E204Q, D205N, E206Q, E209Q) ΔNLS (K82A, R83A, K84A) bottom 5' TCCCCGTACTGAGAGAAGAACTGCCGCAGCTGGTTCTGAGTCATGTTCTGTGTACAGCGCCCCACAAACA 3'	this study	KS2485
TARDBP *PA2-2* (D216N, D219N) ΔNLS (K82A, R83A, K84A) top 5' AGTTCTTCTCTCAGTACGGGAACGTGATGAACGTCTTCATCCCCAAGCCATT 3'	this study	KS2486
TARDBP *PA2-2* (D216N, D219N) ΔNLS (K82A, R83A, K84A) bottom 5' AATGGCTTGGGGATGAAGACGTTCATCACGTTCCCGTACTGAGAGAAGAACT 3'	this study	KS2487
Recombinant DNA		
pMW20(U)-pGAL-GFP	This study	
pMW20(U)-pGAL-GFP-NST1	This study	
pMW20(U)-pGAL-GFP-NST1Δ2-122	This study	
pMW20(U)-pGAL-GFP-NST1Δ123-293	This study	
pMW20(U)-pGAL-GFP-NST1Δ294-459	This study	
pMW20(U)-pGAL-GFP-NST1Δ460-752	This study	
pMW20(U)-pGAL-GFP-NST1Δ460-630	This study	
pMW20(U)-pGAL-GFP-NST1Δ631-752	This study	
pMW20(U)-pGAL-GFP-NST1Δ753-844	This study	
pMW20(U)-pGAL-GFP-NST1Δ845-1015	This study	
pMW20(U)-pGAL-GFP-NST1Δ1016-1240	This study	
pMW20(U)-pGAL-GFP-NST1Δ460-596	This study	
pMW20(U)-pGAL-GFP-EDC3	This study	
pMW20(U)-pGAL-GFP-EDC3Δ65-205	This study	
pMW20(U)-pGAL-GFP-EDC3Δ65-180	This study	
pMW20(U)-pGAL-GFP-EDC3Δ181-205	This study	
pMW20(U)-pGAL-GFP-EDC3Δ330-380	This study	
pMW20(U)-pGAL-GFP-TARDBP	This study	

pMW20(U)-pGAL-GFP-TARDBPΔ2-29	This study	
pMW20(U)-pGAL-GFP-TARDBPΔ197-220	This study	
pMW20(U)-pGAL-GFP-TARDBPΔ255-276	This study	
pMW20(U)-pGAL-GFP-TARDBPΔ255-414	This study	
pMW20(U)-pGAL-GFP-TARDBPΔNLS (K82A, R83A, K84A)	This study	
pMW20(U)-pGAL-GFP-TARDBPΔ2-29ΔNLS (K82A, R83A, K84A)	This study	
pMW20(U)-pGAL-GFP-TARDBPΔ197-220ΔNLS (K82A, R83A, K84A)	This study	
pMW20(U)-pGAL-GFP-TARDBPΔ255-276ΔNLS (K82A, R83A, K84A)	This study	
pMW20(U)-pGAL-GFP-TARDBPΔ255-414ΔNLS (K82A, R83A, K84A)	This study	
pRS306-pNST1-GFP-NST1	This study	
pRS306-pNST1-GFP-NST1Δ460-630	This study	
pRS306-pNST1-GFP-NST1Δ631-752	This study	
pRS306-pNST1-GFP-NST1Δ1016-1240	This study	
pcDNA3.1myc-HisA-GFP-TARDBP	This study	
pcDNA3.1myc-HisA-GFP-TARDBPΔ2-29	This study	
pcDNA3.1myc-HisA-GFP-TARDBPΔ255-276	This study	
pcDNA3.1myc-HisA-GFP-TARDBPΔ255-414	This study	
pcDNA3.1myc-HisA-GFP-TARDBPΔ197-220	This study	
pcDNA3.1myc-HisA -GFP-TARDBPΔNLS(K82A, R83A, K84A)	This study	
pcDNA3.1myc-HisA -GFP-TARDBPΔ2-29ΔNLS(K82A, R83A, K84A)	This study	
pcDNA3.1myc-HisA -GFP-TARDBPΔ197-220ΔNLS(K82A, R83A, K84A)	This study	
pcDNA3.1myc-HisA -GFP-TARDBPΔ255-276ΔNLS(K82A, R83A, K84A)	This study	
pcDNA3.1myc-HisA -GFP-TARDBPΔ255-414ΔNLS(K82A, R83A, K84A)	This study	
pMW20(U)-pGAL-GFP-TARDBP *PA1-1*(E3Q, E9Q, D10N, E11Q) ΔNLS (K82A, R83A, K84A)	This study	
pMW20(U)-pGAL-GFP-TARDBP *PA1-2*(D13N, E14Q, E17Q, E21Q, D22N, D23N) ΔNLS (K82A, R83A, K84A)	This study	
pMW20(U)-pGAL-GFP-TARDBP *PA1-1PA1-2* (E3Q, E9Q, D10N, E11Q, D13N, E14Q, E17Q, E21Q, D22N, D23N) ΔNLS (K82A, R83A, K84A)	This study	
pMW20(U)-pGAL-GFP-TARDBP *PA2-1* (E200Q, D201N, E204Q, D205N, E206Q, E209Q) ΔNLS (K82A, R83A, K84A)	This study	
pMW20(U)-pGAL-GFP-TARDBP *PA2-2* (D216N, D219N) ΔNLS (K82A, R83A, K84A)	This study	

pMW20(U)-pGAL-GFP-TARDBP *PA2-1PA2-2* (E200Q, D201N, E204Q, D205N, E206Q, E209Q, D216N, D219N) ΔNLS (K82A, R83A, K84A)	This study	
Software and algorithms		
AIUPRed – Prediction of Intrinsically Unstructured Proteins	Eötvös Loránd University (ELTE), MTA-ELTE Momentum Bioinformatics Research Group, Hungary	AIUPred
Disopred3	University College London (UCL), Bioinformatics Group	PSIPRED Workbench
PrDOS – Protein Disorder Prediction System	Osaka University, Graduate School of Information Science and Technology	PrDOS - Protein disorder prediction server
PASTA 2.0 – prediction of amyloid structural aggregation	University of Padova, Department of Biomedical Sciences, INFN, Italy	Aggregation Prediction with PASTA
Aggrescan – prediction of “hot spot” of aggregation on polypeptides	Autònoma University of Barcelona, Institute of Biotechnology and Biomedicine, Department of Biochemistry and Molecular Biology, Spain	Aggrescan: Prediction of "hot spots" of aggregation in polypeptides
FELLS – Fast Estimator of Latent Local Structure	BioComputing Up, University of Padua, Italy	FELLS > Submit
GraphPad Prism 5	GraphPad	https://www.graphpad.com/
GraphPad Prism 10	GraphPad	https://www.graphpad.com/

ImageJ	Schindelin et al. Fiji: an open-source platform for biological-image analysis. *Nat. Methods.* 2012; 9: 676-682	https://imagej.nih.gov/ij/
Custom Python scripts	This paper	Available upon request
Other		
1.8 ml bead-beating tube	SIMPORT, Canada	Cat# T335-6SPR
Acid-washed 0.5 mm bead	Biospec, USA	Cat# 11079105
Polyvinylidene difluoride (PVDF) membrane	Merk Millipore, USA	Cat# IPVH00010

METHOD DETAILS

Yeast cell culture and transformation

Saccharomyces cerevisiae yeast cells were grown in YPAD medium until reaching the exponential growth phase (OD_{600} 0.5). Cells were harvested by centrifugation at 4,000 rpm for 5 min at room temperature (RT). The cell pellet was gently resuspended in 1 mL of 0.1 M LiOAc (Sigma-Aldrich, USA, L6883-250G) and incubated at RT for 5 min, followed by another centrifugation under the same condition. For transformation, cells were gently resuspended in 360 µL of yeast transformation mixture consisting of 50% polyethylene glycol (Sigma-Aldrich, USA, P4338-500G), 1 M LiOAc, 2 mg/mL salmon sperm DNA (Sigma, USA, D1626), and ddH_2O. 100 ng plasmid DNA was added to the cell suspension, and the mixture was incubated at RT for 30 min. Heat shock was performed by incubating the cells at 42°C for 30 min, followed by cooling at RT for 3 min. Cells were harvested again by centrifugation at 4,000 rpm for 5 min at RT, and plated onto SC-Ura plates. Plates were incubated at 25°C until colonies appeared typically 2–3 days.

Protein overexpression in yeast

The cells transformed with plasmids containing NST1, EDC3, *TARDBP* and their deletion mutants were cultured in a SC-U + 2% glucose medium up to the exponential growth phase (OD_{600} 0.5) and harvested. The cells were washed with a SC-U + 2% raffinose + 0.1% glucose medium three times, diluted to half its concentration, and cultured for an additional 3 hours in SC-U + 2% raffinose + 0.1% glucose. Thereafter, galactose was added to a final 2% concentration and incubated for designated hours.

1,6-Hexanediol treatment of yeast

Yeast cells induced for protein overexpression in 2% galactose for 4 hours were harvested by centrifugation at 4000 rpm for 5 minutes, and the resulting pellet was collected. The cell pellet was then resuspended and incubated in SC-U medium supplemented with 2% galactose, 2% raffinose, 0.1% glucose, and 10% 1,6-hexanediol (Daejung Chemical & Metals Co., LTD, South Korea, 629-11-8) for 1 hour.

Chromosomal integration of genes in yeast

Various NST1 deletion mutants were acquired by PCR-mediated deletion cloning with the full length pRS306-pNST1-NST1 and verified by sequencing. Plasmids pRS306-pNST1-NST1 and its deletion mutants were treated with EcoRV to make a single cut at the URA3 and were transformed into *Δnst1* cells (YSK3490) by 42 ˚C heat shock. Integration into the chromosome occurred at low frequency via homologous recombination at the URA3. The transformed cells were plated on the SC plate without uracil and colony PCR was performed to confirm whether the fragment was successfully transformed.

Infusion cloning of genes

The PCR-amplified coding sequences were generated using primers containing 15-bp extensions homologous to the vector ends. The destination vector pcDNA3.1-myc-His was linearized by restriction enzyme digestion at 37°C for 3 h. The digested vector and PCR fragments were then subjected to infusion cloning reaction (EZ-HT cloning kit, Enzynomics, Korea, EZ016TM), which utilizes single-strand annealing activity to join DNA fragments with complementary ends, circumventing the need for conventional ligation. The reaction products were transformed into chemically competent *E. coli* DH5α

cells, and transformants were selected on LB agar plates supplemented with ampicillin (100 µg/ml). The integrity of the resulting constructs was verified by DNA sequencing.

TDP-43 PA1 and PA2 Domain Mutagenesis

PCR-based site-directed mutagenesis was performed using the plasmid pMW20(U)-pGAL-GFP-TARDBPΔNLS (K82A, R83A, K84A) as a template to introduce targeted amino acid substitutions within the TDP-43 PA1 and PA2 domain. The *PA1-1* mutant was generated with primers KS2492 and KS2493, and the *PA1-2* mutant with KS2494 and KS2495. The *PA2-1* mutant was generated with primers KS2484 and KS2485, and the *PA2-2* mutant with primers KS2486 and KS2487. The *PA1-1PA1-2* and *PA2-1PA2-2* mutants, which harbor both the *PA1-1* and *PA1-2* mutations or *PA2-1* and *PA2-2* mutations, were constructed using the *PA1-2* or *PA2-1* plasmid as a template with the *PA1-1PA1-2* primers (KS2500 and KS2501) or the *PA2-2* primers (KS2486 and KS2487), respectively. The sequences of all primers were listed in the KEY RESOURCES TABLE. All mutant strains were verified by DNA sequencing.

Widefield microscopy of cells and image analysis

GFP-labeled proteins expressed in the cells were visualized using an Axioplan2 microscope (Carl Zeiss,Jena, Germany) equipped with a 100x Plan-Neofluar oil immersion objective. Consistent culture conditions, exposure times, and fluorescence intensities were maintained across all strains in this study to ensure a comparative analysis of puncta intensity. Image analysis was performed using FIJI ImageJ (https://imagej.nih.gov/ij/).

Confocal microscopy of cells and image analysis

GFP-labeled proteins expressed in the cells were imaged using both a ZEISS LSM900 laser scanning confocal microscope (Carl Zeiss, Jena, Germany) equipped with high-sensitivity GaAsP-PMT detectors (2 standard and 1 additional GaAsP-PMT), and a ZEISS LSM980 confocal microscope with an Airyscan 2 detector (Carl Zeiss, Jena, Germany). For Airyscan super-resolution imaging with the LSM980, the Airyscan Joint Deconvolution mode was utilized, achieving lateral resolution down to ~90 nm. Both systems were fitted with a 63x/1.4 NA oil immersion objective, and all images were acquired at room temperature. Microscope settings, including laser power, detector gain, and pinhole size, were kept

identical for all samples to ensure quantitative comparability. Image acquisition and processing were performed using ZEISS Zen software (version 3.9, Carl Zeiss).

FCS measurements and data analysis

All FCS measurements were performed at 25°C on a confocal microscope (LSM780; Carl Zeiss, Inc. Germany) combined with a ConfoCor3 and a 40×/1.2 NA water-immersion objective (Carl Zeiss, Inc.). Details of the analysis of fluorescence auto-correlation functions (FAFs) were described in the previous study (Kawai-Noma et al., 2006; Pack et al., 2014), FAFs were fitted to a two-component model with a triplet term.

For each cell, the cytoplasmic region was identified by visual inspection of the fluorescence image, avoiding the GFP visualized puncta. At least five independent measurements (each lasting 10 s) were recorded per cell. Over 15 cells were analyzed per condition.

Autocorrelation curves were generated using ZEN black software (Carl Zeiss, Inc.) and fitted with two-component 3D diffusion model including a triplet term:

$$G_x(\tau) = 1 + \frac{1}{N}\sum_i F_i(1+\frac{\tau}{\tau_i})^{-1}(1+\frac{\tau}{s^2\tau_i})^{-1/2}$$

Where F_i and τ_i are the fraction and diffusion time of component I, respectively; N is the average number of fluorescent molecules in the confocal volume defined by the radius w_0 and the length $2z_0$; and s is the structure parameter representing the ratio $s = z_0/w_0$ (axial/lateral radius ratio of the confocal volume). The structural parameter was calibrated using a known concentration of Rh6G standard solution at room temperature. The relationship between absolute concentration and calculated N was calibrated using a known concentration of Rh6G or recombinant mGFP solution. The effect of photobleaching on evaluation of concentration was determined according to a previous study. Fluoprescence correlation functions (FCFs) in live cells were measured sequentially 6 times with duration of 10s to minimize photobleaching effect.

The cytoplasmic concentration of the target protein was calculated as

$$C = \frac{N}{N_A V_{eff}}$$

Where N_A is Avogadro's number and V_{eff} is the effective confocal volume determined from calibration measurements with Rhodamine 6G solutdion.

Yeast cell lysis and RNase inhibitor treatment

For primary culture, yeast cells were inoculated and grown for 24 h at 25ºC in 10 ml of SC media (w/ 2% glucose). After 24 h, the primary cultured cells were diluted to 0.1 optical density (O.D.) value in 100 ml of the same media and cultured for 30 h at 25ºC. 50 ml of cells were then collected in 1.8 ml bead-beating tubes (SIMPORT, Canada, #T335-6SPR). In each tube, we added 200 µl of acid-washed 0.5 mm bead (Biospec, USA, #11079105) and 400 µl of pH 7.4 PBS lysis buffer with 0.1% NP40 (BIO BASIC, Canada, #NDB0385), cOmplete™ mini EDTA-free Protease Inhibitor Cocktail (Roche, Switzerland, #11836170001), 1 mM DTT (Georgiachem, USA, #DT1050), 1 mM PMSF (Georgiachem, USA, #PS2064), and 10 mM Ribonucleoside vanadyl complex (RVC, NEW ENGLAND Biolabs, USA, #S1402S), a transition state analog acting as a non-covalently bound ribonuclease (RNase) inhibitor. These tubes were incubated on ice for 15 min and then lysed by the bead beater for 4 times of a cycle set of 30 sec beating and 8 min rest. The crude extracts were centrifuged at 2000 g for 5 min at 4ºC. These separated supernatants were centrifuged again at 10,000 g for 10 min at 4ºC. To obtain the pellets, all the supernatants were carefully removed. More than 5 fluorescent images of these pellets were acquired by fluorescent microscopy.

Fluorescence recovery after photobleaching (FRAP) in living yeast cells

Fluorescence recovery after photobleaching (FRAP) was performed on puncta induced by GAL promoter using a Zeiss LSM900 laser scanning confocal microscope with a 100×/1.40 NA oil immersion objective (Carl Zeiss AG, Oberkochen, Germany). Cells were mounted on agarose pads, composed of SC 2% raffinose/ 2% galactose media and 1~3% agarose, to minimize the delicate movements of cells. For the confocal imaging, 0.6% 488 nm wavelength laser and GaAsP-PMT detector were used. Due to the low GFP signals of proteins and the small size of yeast, the pinhole was opened to 3 Airy units, about 240 µm. For fast imaging, the acquisition mode was set to 512 px X 512 px frame size, 8 bits per pixel, 9

(about 1 μs of pixel times) scan speed, one-way, and none averaging scanning. For the FRAP experiments, the region of interest (ROI) was selected, and 200 cycles with no interval of time series were set. After snapping five images, bleaching on ROI was performed repeatedly three times with the power of 10~100% 488 nm laser beam. Bleached signals on ROI were recovered, and these signals were acquired for the left 194 cycles. All the experiment was repeated about 20~30 foci of each strain. If the foci were out of focus for 200 cycles, these data were discarded.

Image analysis for FRAP

The mean intensity in ROI at each cycle was analyzed and drawn as graphs using Fiji with the Stowers plugin. All the graphs were normalized to 0-1, and the average curves of these graphs were calculated with GraphPad Prism 10 (GraphPad Software, CA, USA). These normalized curves were fitted with Eq.1.

$$y = y_{max} \times (1 - e^{-\frac{t}{\tau}}) \quad (1)$$

In Eq.1, y_{max} is the y value at infinite time ($t \approx \infty$), and τ (tau) is the time point when the y value is equal to 63.2% of y_{max} value. The first derivative functions of the fitted curves were analyzed with GraphPad Prism 10 to calculate the maximum velocity of the recovery curves.

Fixation and DAPI staining of yeast cells

Following 4 hours of galactose-mediated induction, yeast cells were harvested by centrifugation at 4,000 rpm for 5 minutes at RT. The supernatant was carefully removed, and cell pellets were resuspended in 4% paraformaldehyde (PFA) dissolved in Dulbecco's phosphate-buffered saline (DPBS) (T&I, South Korea, BPP-9004) for fixation by gentle inversion mixing for 1 h at RT. To remove residual PFA, cells were subjected to two successive wash cycles consisting of centrifugation (4,000 rpm, 2 minutes) and resuspension in fresh DPBS (Welgene, South Korea, LB 001-02). The final cell pellet was reconstituted in DPBS and evenly distributed onto microscope slides. Vectashield mounting medium for fluorescence with DAPI (Vector Laboratories, Inc., USA, H-1200) was applied to each sample, followed by gentle mixing using a pipette tip to ensure homogeneous distribution of cells. Cellular morphology and fluorescence signals were subsequently analyzed using a Axioplan2 microscope (Carl Zeiss, Jena, Germany) equipped with a DAPI-specific filter set.

U2OS cell culture and transfection

U2OS cells (ATCC, CRL-1427, HTB 96, Manassas, VA, USA) were cultured in Dulbecco's Modified Eagle Medium (DMEM with high glucose; Cytiva, USA SH30023.01) supplemented with 10% fetal bovine serum (FBS; Cytiva, USA, SH30088.03) and 1X antibiotic-antimycotic solution (Anti-Anti; Gibco, USA ,15240-062) at 37°C in a humidified incubator with 5% CO_2. Once the cells reached 70% confluence, they were transfected with pcDNA3.1-myc-hisA expression vectors encoding GFP-TDP-43 and its IDR deletion mutants using Lipofectamine 3000 (Invitrogen, USA, L300015), following the manufacturer's protocol. After transfection, the cells were selected with 600 ng/μL Geneticin™ Selective Antibiotic (G418 Sulfate) (Gibco, USA, 10131035) .

Fixation and DAPI staining of U2OS cells

Forty-eight hours after transfection, U2OS cells cultured on a cover slide were fixed with 4% paraformaldehyde (PFA, T&I, South Korea, BPP-9004) at RT for 1 h, washed three times with phosphate-buffered saline (PBS, WELGENE, South Korea, LB 001-02)., and mounted using a DAPI-containing mounting solution (Vector Laboratories, Inc., USA, H-1200). Fluorescence images were acquired using an Axioplan2 fluorescence microscope (Carl Zeiss, Jena, Germany) equipped with a 20x/0.5 Ph2 Plan-Neofluar objective.

Western blotting analysis

Protein extraction from yeast cells was obtained using the alkaline lysis as described in Choi and Song (*Int. J. Mol. Sci. 2022*, *23*, 2501) U2OS cell extract was obtained as previously described (PLOS ONE | https://doi.org/10.1371/journal.pone.0302936 May 7, 2024). Protein samples were separated by sodium dodecyl sulfate–polyacrylamide gel electrophoresis (SDS-PAGE) and transferred onto polyvinylidene difluoride (PVDF) membranes (Merck Millipore, Burlington, MA, USA) using a semi-dry transfer system. Anti-GFP antibody (600-101-215 ROCKLAND, Limerick, PA, USA, 1:1000 dilution) was used for Western blotting. To confirm equal protein loading, the membranes were stripped of the anti-GFP antibody prior to re-probing with an anti-Tubulin antibody anti-Tubulin (Mouse, Sigma-Aldrich, Cat# T5168, 1:10000

dilution) and subsequently with HRP-conjugated anti-mouse secondary antibody (Santa Cruz Biotechnology, Cat# sc-2005, 1:10000 dilution).

QUANTIFICATION AND STATISTICAL ANALYSIS

Only statistically analyzed data are shown as mean ± SEM. Statistical analyses were performed using GraphPad Prism. Statistical significance was determined using unpaired two-tailed Student's t-test with Welch's correction. $P < 0.05$ was considered statistically significant.

DATA AND CODE AVAILABILITY

Custom algorithms were implemented in Python 3.10 by the authors. The analysis pipeline included modules written with NumPy and SciPy and was used to process experimental data shown in Figure 1. The code used in this study was written by the authors and is available from the corresponding author upon reasonable request.

ADDITIONAL RESOURCES

N/A

ACKNOWLEDGMENTS

We thank the Cellular Imaging Core Facility at the ConveRgence mEDIcine research cenTer (CREDIT), Asan Medical Center, for technical support. The authors would like to thank Ewha Women's University Fluorescence Core Imaging Center for valuable guidance in FRAP analysis. We specially appreciate the technical assistance provided by professor Dongmin Kang, the Director, and Research Technician Sinae Jang, of Ewha Fluorescence Core Imaging Center. TDP-43 gene clone was kindly provided by Dr. Hyung-Jun Kim in Korea Brain Research Institute. This work was in part supported by the National Research Foundation of Korea (NRF) grant provided to K. Song (RS-2023-00243284).

AUTHOR CONTRIBUTIONS

Conceptualization, K.S. and Y.J.C.; methodology, K.S., Y.J.C, and C.P.; Investigation, Y.J.C, Y.L., S.C., and Y.P.; writing—original draft, K.S. and Y.J.C.; writing—review & editing, K.S., Y.J.C, C.P, and Y.J.; funding acquisition, K.S.; resources, K.S. and C.K.B.; supervision, K.S., and Y.J.C

DECLARATION OF INTERESTS

The authors (K.S., Y.J.C., S.C., and Y.P.) have applied for a patent entitled "Specific Amino Acid Sequence Deletion Mutants for Inhibiting TDP-43 Aggregation Causing Degenerative Brain Diseases, and Method for Identifying Mutant Sequences (DP 2025-0349)" with the Korean Intellectual Property Office. The authors declare no other competing interests.

REFERENCES

Ahmad, A., Uversky, V.N., and Khan, R.H. (2022). Aberrant liquid-liquid phase separation and amyloid aggregation of proteins related to neurodegenerative diseases. Int J Biol Macromol *220*, 703-720. 10.1016/j.ijbiomac.2022.08.132.

Alberti, S., and Hyman, A.A. (2021). Biomolecular condensates at the nexus of cellular stress, protein aggregation disease and ageing. Nat Rev Mol Cell Biol *22*, 196-213. 10.1038/s41580-020-00326-6.

Alshareedah, I., Borcherds, W.M., Cohen, S.R., Singh, A., Posey, A.E., Farag, M., Bremer, A., Strout, G.W., Tomares, D.T., Pappu, R.V., et al. (2024). Sequence-specific interactions determine viscoelasticity and aging dynamics of protein condensates. Nat Phys *20*, 1482-1491. 10.1038/s41567-024-02558-1.

Alshareedah, I., Moosa, M.M., Pham, M., Potoyan, D.A., and Banerjee, P.R. (2021). Programmable viscoelasticity in protein-RNA condensates with disordered sticker-spacer polypeptides. Nat Commun *12*, 6620. 10.1038/s41467-021-26733-7.

Banani, S.F., Afeyan, L.K., Hawken, S.W., Henninger, J.E., Dall'Agnese, A., Clark, V.E., Platt, J.M., Oksuz, O., Hannett, N.M., Sagi, I., et al. (2022). Genetic variation associated with condensate dysregulation in disease. Dev Cell *57*, 1776-1788 e1778. 10.1016/j.devcel.2022.06.010.

Banani, S.F., Lee, H.O., Hyman, A.A., and Rosen, M.K. (2017). Biomolecular condensates: organizers of cellular biochemistry. Nat Rev Mol Cell Biol *18*, 285-298. 10.1038/nrm.2017.7.

Banerjee, D.S., Chigumira, T., Lackner, R.M., Kratz, J.C., Chenoweth, D.M., Banerjee, S., and Zhang, H. (2024). Interplay of condensate material properties and chromatin heterogeneity governs nuclear condensate ripening. bioRxiv. 10.1101/2024.05.07.593010.

Banjade, S., and Rosen, M.K. (2014). Phase Transitions of Multivalent Proteins Can Promote Clustering of Membrane Receptors. Elife *3*. ARTN e04123

10.7554/eLife.04123.

Biswas, S., and Potoyan, D.A. (2024). Decoding Biomolecular Condensate Dynamics: An Energy Landscape Approach. bioRxiv. 10.1101/2024.09.24.614805.

775 Borcherds, W., Bremer, A., Borgia, M.B., and Mittag, T. (2021). How do intrinsically disordered protein
776 regions encode a driving force for liquid-liquid phase separation? Curr Opin Struc Biol *67*, 41-50.
777 10.1016/j.sbi.2020.09.004.
778 Chen, C., Yamanaka, Y., Ueda, K., Li, P., Miyagi, T., Harada, Y., Tezuka, S., Narumi, S., Sugimoto, M.,
779 Kuroda, M., et al. (2021). Phase separation and toxicity of C9orf72 poly(PR) depends on alternate
780 distribution of arginine. J Cell Biol *220*. 10.1083/jcb.202103160.
781 Chien, H.M., Lee, C.C., and Huang, J.J. (2021). The Different Faces of the TDP-43 Low-Complexity
782 Domain: The Formation of Liquid Droplets and Amyloid Fibrils. Int J Mol Sci *22*. 10.3390/ijms22158213.
783 Choi, C.H., Lee, D.S.W., Sanders, D.W., and Brangwynne, C.P. (2024). Condensate interfaces can
784 accelerate protein aggregation. Biophysical Journal *123*, 1404-1413. 10.1016/j.bpj.2023.10.009.
785 Choi, J.M., Holehouse, A.S., and Pappu, R.V. (2020). Physical Principles Underlying the Complex Biology
786 of Intracellular Phase Transitions. Annu Rev Biophys *49*, 107-133. 10.1146/annurev-biophys-121219-
787 081629.
788 Choi, Y.J., Lee, Y., Lin, Y., Heo, Y., Lee, Y.H., and Song, K. (2022). The Multivalent Polyampholyte Domain
789 of Nst1, a P-Body-Associated Saccharomyces cerevisiae Protein, Provides a Platform for Interacting with
790 P-Body Components. Int J Mol Sci *23*. 10.3390/ijms23137380.
791 Cohen, L.S., Mikhli, C., Jiao, X., Kiledjian, M., Kunkel, G., and Davis, R.E. (2005). Dcp2 Decaps
792 m2,2,7GpppN-capped RNAs, and its activity is sequence and context dependent. Mol Cell Biol *25*, 8779-
793 8791. 10.1128/MCB.25.20.8779-8791.2005.
794 Dickson, Z.W., and Golding, G.B. (2022). Low Complexity Regions in Mammalian Proteins are Associated
795 with Low Protein Abundance and High Transcript Abundance. Mol Biol Evol *39*.
796 10.1093/molbev/msac087.
797 Fondon, J.W., 3rd, and Garner, H.R. (2004). Molecular origins of rapid and continuous morphological
798 evolution. Proc Natl Acad Sci U S A *101*, 18058-18063. 10.1073/pnas.0408118101.
799 Fushimi, K., Long, C., Jayaram, N., Chen, X., Li, L., and Wu, J.Y. (2011). Expression of human FUS/TLS in
800 yeast leads to protein aggregation and cytotoxicity, recapitulating key features of FUS proteinopathy.
801 Protein Cell *2*, 141-149. 10.1007/s13238-011-1014-5.
802 Gao, G., Sumrall, E.S., Pitchiaya, S., Bitzer, M., Alberti, S., and Walter, N.G. (2023). Biomolecular
803 condensates in kidney physiology and disease. Nat Rev Nephrol *19*, 756-770. 10.1038/s41581-023-
804 00767-0.
805 Gruijs da Silva, L.A., Simonetti, F., Hutten, S., Riemenschneider, H., Sternburg, E.L., Pietrek, L.M., Gebel,
806 J., Dotsch, V., Edbauer, D., Hummer, G., et al. (2022). Disease-linked TDP-43 hyperphosphorylation
807 suppresses TDP-43 condensation and aggregation. EMBO J *41*, e108443. 10.15252/embj.2021108443.
808 Hurtle, B.T., Xie, L., and Donnelly, C.J. (2023). Disrupting pathologic phase transitions in
809 neurodegeneration. J Clin Invest *133*. 10.1172/JCI168549.
810 Johnson, B.S., McCaffery, J.M., Lindquist, S., and Gitler, A.D. (2008). A yeast TDP-43 proteinopathy
811 model: Exploring the molecular determinants of TDP-43 aggregation and cellular toxicity. Proc Natl Acad
812 Sci U S A *105*, 6439-6444. 10.1073/pnas.0802082105.
813 Kawai-Noma, S., Ayano, S., Pack, C.G., Kinjo, M., Yoshida, M., Yasuda, K., and Taguchi, H. (2006).
814 Dynamics of yeast prion aggregates in single living cells. Genes Cells *11*, 1085-1096. 10.1111/j.1365-
815 2443.2006.01004.x.
816 Kellett, E.A., Bademosi, A.T., and Walker, A.K. (2025). Molecular mechanisms and consequences of TDP-
817 43 phosphorylation in neurodegeneration. Mol Neurodegener *20*, 53. 10.1186/s13024-025-00839-8.
818 Lange, S.S., and Vasquez, K.M. (2009). HMGB1: the jack-of-all-trades protein is a master DNA repair
819 mechanic. Mol Carcinog *48*, 571-580. 10.1002/mc.20544.
820 Lee, D.S.W., Wingreen, N.S., and Brangwynne, C.P. (2021). Chromatin Mechanics Dictates Subdiffusion
821 and Coarsening Dynamics of Embedded Condensates. Biophysical Journal *120*, 318a-318a.

822 Li, Q., Babinchak, W.M., and Surewicz, W.K. (2021). Cryo-EM structure of amyloid fibrils formed by the
823 entire low complexity domain of TDP-43. Nat Commun *12*, 1620. 10.1038/s41467-021-21912-y.
824 Linsenmeier, M., Faltova, L., Morelli, C., Capasso Palmiero, U., Seiffert, C., Kuffner, A.M., Pinotsi, D.,
825 Zhou, J., Mezzenga, R., and Arosio, P. (2023). The interface of condensates of the hnRNPA1 low-
826 complexity domain promotes formation of amyloid fibrils. Nat Chem *15*, 1340-1349. 10.1038/s41557-
827 023-01289-9.
828 Linsenmeier, M., Kopp, M.R.G., Stavrakis, S., de Mello, A., and Arosio, P. (2021). Analysis of biomolecular
829 condensates and protein phase separation with microfluidic technology. Biochim Biophys Acta Mol Cell
830 Res *1868*, 118823. 10.1016/j.bbamcr.2020.118823.
831 Lu, B., Qiu, R., Wei, J., Wang, L., Zhang, Q., Li, M., Zhan, X., Chen, J., Hsieh, I.Y., Yang, C., et al. (2024).
832 Phase separation of phospho-HDAC6 drives aberrant chromatin architecture in triple-negative breast
833 cancer. Nat Cancer. 10.1038/s43018-024-00816-y.
834 Lu, S., Hu, J., Arogundade, O.A., Goginashvili, A., Vazquez-Sanchez, S., Diedrich, J.K., Gu, J., Blum, J.,
835 Oung, S., Ye, Q., et al. (2022). Heat-shock chaperone HSPB1 regulates cytoplasmic TDP-43 phase
836 separation and liquid-to-gel transition. Nat Cell Biol *24*, 1378-1393. 10.1038/s41556-022-00988-8.
837 Mehta, S., and Zhang, J. (2022). Liquid-liquid phase separation drives cellular function and dysfunction in
838 cancer. Nat Rev Cancer *22*, 239-252. 10.1038/s41568-022-00444-7.
839 Mensah, M.A., Niskanen, H., Magalhaes, A.P., Basu, S., Kircher, M., Sczakiel, H.L., Reiter, A.M.V., Elsner,
840 J., Meinecke, P., Biskup, S., et al. (2023). Aberrant phase separation and nucleolar dysfunction in rare
841 genetic diseases. Nature *614*, 564-571. 10.1038/s41586-022-05682-1.
842 Miyagi, T., Yamazaki, R., Ueda, K., Narumi, S., Hayamizu, Y., Uji, I.H., Kuroda, M., and Kanekura, K.
843 (2022). The Patterning and Proportion of Charged Residues in the Arginine-Rich Mixed-Charge Domain
844 Determine the Membrane-Less Organelle Targeted by the Protein. Int J Mol Sci *23*.
845 10.3390/ijms23147658.
846 Nam, J., and Gwon, Y. (2023). Neuronal biomolecular condensates and their implications in
847 neurodegenerative diseases. Front Aging Neurosci *15*, 1145420. 10.3389/fnagi.2023.1145420.
848 Niedner-Boblenz, A., Monecke, T., Hennig, J., Klostermann, M., Hofweber, M., Davydova, E., Gerber,
849 A.P., Anosova, I., Mayer, W., Muller, M., et al. (2024). Intrinsically disordered RNA-binding motifs
850 cooperate to catalyze RNA folding and drive phase separation. Nucleic Acids Res *52*, 14205-14228.
851 10.1093/nar/gkae1107.
852 Niu, X., Zhang, L., Wu, Y., Zong, Z., Wang, B., Liu, J., Zhang, L., and Zhou, F. (2023). Biomolecular
853 condensates: Formation mechanisms, biological functions, and therapeutic targets. MedComm (2020) *4*,
854 e223. 10.1002/mco2.223.
855 Oiwa, K., Watanabe, S., Onodera, K., Iguchi, Y., Kinoshita, Y., Komine, O., Sobue, A., Okada, Y., Katsuno,
856 M., and Yamanaka, K. (2023). Monomerization of TDP-43 is a key determinant for inducing TDP-43
857 pathology in amyotrophic lateral sclerosis. Sci Adv *9*, eadf6895. 10.1126/sciadv.adf6895.
858 Outeiro, T.F., and Lindquist, S. (2003). Yeast cells provide insight into alpha-synuclein biology and
859 pathobiology. Science *302*, 1772-1775. 10.1126/science.1090439.
860 Pack, C.G. (2021). Application of quantitative cell imaging using label-free optical diffraction
861 tomography. Biophys Physicobiol *18*, 244-253. 10.2142/biophysico.bppb-v18.027.
862 Pack, C.G., Yukii, H., Toh-e, A., Kudo, T., Tsuchiya, H., Kaiho, A., Sakata, E., Murata, S., Yokosawa, H.,
863 Sako, Y., et al. (2014). Quantitative live-cell imaging reveals spatio-temporal dynamics and cytoplasmic
864 assembly of the 26S proteasome. Nat Commun *5*, 3396. 10.1038/ncomms4396.
865 Ranganathan, S., Liu, J., and Shakhnovich, E. (2022). Different states and the associated fates of
866 biomolecular condensates. Essays Biochem *66*, 849-862. 10.1042/EBC20220054.
867 Regy, R.M., Dignon, G.L., Zheng, W., Kim, Y.C., and Mittal, J. (2020). Sequence dependent phase
868 separation of protein-polynucleotide mixtures elucidated using molecular simulations. Nucleic Acids Res
869 *48*, 12593-12603. 10.1093/nar/gkaa1099.

870 Saar, K.L., Morgunov, A.S., Qi, R., Arter, W.E., Krainer, G., Lee, A.A., and Knowles, T.P.J. (2021). Learning
871 the molecular grammar of protein condensates from sequence determinants and embeddings. Proc Natl
872 Acad Sci U S A *118*. 10.1073/pnas.2019053118.
873 Saitoh, N., Spahr, C.S., Patterson, S.D., Bubulya, P., Neuwald, A.F., and Spector, D.L. (2004). Proteomic
874 analysis of interchromatin granule clusters. Mol Biol Cell *15*, 3876-3890. 10.1091/mbc.e04-03-0253.
875 Sanfeliu-Cerdan, N., Catala-Castro, F., Mateos, B., Garcia-Cabau, C., Ribera, M., Ruider, I., Porta-de-la-
876 Riva, M., Canals-Calderon, A., Wieser, S., Salvatella, X., and Krieg, M. (2023). A MEC-2/stomatin
877 condensate liquid-to-solid phase transition controls neuronal mechanotransduction during touch
878 sensing. Nat Cell Biol *25*, 1590-1599. 10.1038/s41556-023-01247-0.
879 Schneider-Poetsch, T., Ju, J., Eyler, D.E., Dang, Y., Bhat, S., Merrick, W.C., Green, R., Shen, B., and Liu, J.O.
880 (2010). Inhibition of eukaryotic translation elongation by cycloheximide and lactimidomycin. Nat Chem
881 Biol *6*, 209-217. 10.1038/nchembio.304.
882 Shen, Y., Chen, A., Wang, W., Shen, Y., Ruggeri, F.S., Aime, S., Wang, Z., Qamar, S., Espinosa, J.R.,
883 Garaizar, A., et al. (2023). The liquid-to-solid transition of FUS is promoted by the condensate surface.
884 Proc Natl Acad Sci U S A *120*, e2301366120. 10.1073/pnas.2301366120.
885 Shenoy, J., Lends, A., Berbon, M., Bilal, M., El Mammeri, N., Bertoni, M., Saad, A., Morvan, E., Grelard, A.,
886 Lecomte, S., et al. (2023). Structural polymorphism of the low-complexity C-terminal domain of TDP-43
887 amyloid aggregates revealed by solid-state NMR. Front Mol Biosci *10*, 1148302.
888 10.3389/fmolb.2023.1148302.
889 Sim, K.L., and Creamer, T.P. (2002). Abundance and distributions of eukaryote protein simple sequences.
890 Mol Cell Proteomics *1*, 983-995. 10.1074/mcp.m200032-mcp200.
891 Sneideriene, G., Gonzalez Diaz, A., Adhikari, S.D., Wei, J., Michaels, T., Sneideris, T., Linse, S.,
892 Vendruscolo, M., Garai, K., and Knowles, T.P.J. (2025). Lipid-induced condensate formation from the
893 Alzheimer's Abeta peptide triggers amyloid aggregation. Proc Natl Acad Sci U S A *122*, e2401307122.
894 10.1073/pnas.2401307122.
895 Sood, A., and Zhang, B. (2024). Preserving condensate structure and composition by lowering sequence
896 complexity. Biophys J *123*, 1815-1826. 10.1016/j.bpj.2024.05.026.
897 Sun, Z., Diaz, Z., Fang, X., Hart, M.P., Chesi, A., Shorter, J., and Gitler, A.D. (2011). Molecular
898 determinants and genetic modifiers of aggregation and toxicity for the ALS disease protein FUS/TLS.
899 PLoS Biol *9*, e1000614. 10.1371/journal.pbio.1000614.
900 Sundaravadivelu Devarajan, D., Wang, J., Szala-Mendyk, B., Rekhi, S., Nikoubashman, A., Kim, Y.C., and
901 Mittal, J. (2024). Sequence-dependent material properties of biomolecular condensates and their
902 relation to dilute phase conformations. Nat Commun *15*, 1912. 10.1038/s41467-024-46223-w.
903 Teixeira, D., Sheth, U., Valencia-Sanchez, M.A., Brengues, M., and Parker, R. (2005). Processing bodies
904 require RNA for assembly and contain nontranslating mRNAs. RNA *11*, 371-382. 10.1261/rna.7258505.
905 Tibble, R.W., Depaix, A., Kowalska, J., Jemielity, J., and Gross, J.D. (2021). Biomolecular condensates
906 amplify mRNA decapping by biasing enzyme conformation. Nat Chem Biol *17*, 615-623. 10.1038/s41589-
907 021-00774-x.
908 Ukmar-Godec, T., Hutten, S., Grieshop, M.P., Rezaei-Ghaleh, N., Cima-Omori, M.S., Biernat, J.,
909 Mandelkow, E., Soding, J., Dormann, D., and Zweckstetter, M. (2019). Lysine/RNA-interactions drive and
910 regulate biomolecular condensation. Nat Commun *10*, 2909. 10.1038/s41467-019-10792-y.
911 Van Treeck, B., and Parker, R. (2018). Emerging Roles for Intermolecular RNA-RNA Interactions in RNP
912 Assemblies. Cell *174*, 791-802. 10.1016/j.cell.2018.07.023.
913 Visser, B.S., Lipinski, W.P., and Spruijt, E. (2024). The role of biomolecular condensates in protein
914 aggregation. Nat Rev Chem *8*, 686-700. 10.1038/s41570-024-00635-w.
915 Wang, A., Conicella, A.E., Schmidt, H.B., Martin, E.W., Rhoads, S.N., Reeb, A.N., Nourse, A., Ramirez
916 Montero, D., Ryan, V.H., Rohatgi, R., et al. (2018a). A single N-terminal phosphomimic disrupts TDP-43
917 polymerization, phase separation, and RNA splicing. EMBO J *37*. 10.15252/embj.201797452.

Wang, B., Zhang, L., Dai, T., Qin, Z., Lu, H., Zhang, L., and Zhou, F. (2021). Liquid-liquid phase separation in human health and diseases. Signal Transduct Target Ther *6*, 290. 10.1038/s41392-021-00678-1.

Wang, J., Choi, J.M., Holehouse, A.S., Lee, H.O., Zhang, X., Jahnel, M., Maharana, S., Lemaitre, R., Pozniakovsky, A., Drechsel, D., et al. (2018b). A Molecular Grammar Governing the Driving Forces for Phase Separation of Prion-like RNA Binding Proteins. Cell *174*, 688-699 e616. 10.1016/j.cell.2018.06.006.

Wang, X., Bigman, L.S., Greenblatt, H.M., Yu, B., Levy, Y., and Iwahara, J. (2023). Negatively charged, intrinsically disordered regions can accelerate target search by DNA-binding proteins. Nucleic Acids Res *51*, 4701-4712. 10.1093/nar/gkad045.

Figure 1

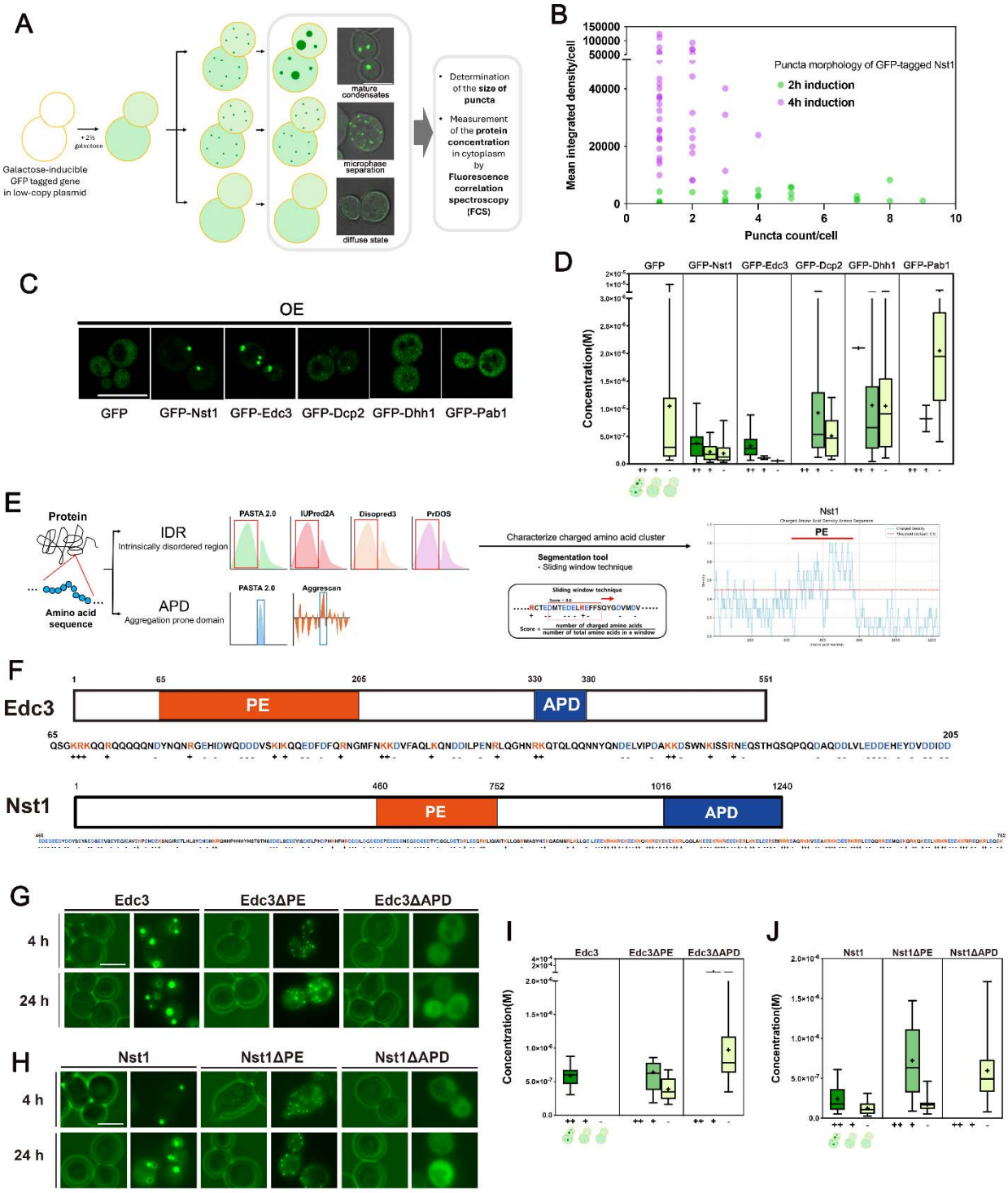
A
Galactose-inducible GFP tagged gene in low-copy plasmid
+2% galactose
mature condensates
microphase separation
diffuse state
Determination of the size of puncta
Measurement of the protein concentration in cytoplasm by Fluorescence correlation spectroscopy (FCS)
B
Mean integrated density/cell
Puncta count/cell
Puncta morphology of GFP-tagged Nst1
2h induction
4h induction
C
OE
GFP
GFP-Nst1
GFP-Edc3
GFP-Dcp2
GFP-Dhh1
GFP-Pab1
D
Concentration(M)
E
Protein
IDR
Intrinsically disordered region
APD
Aggregation prone domain
Amino acid sequence
PASTA 2.0
IUPred2A
Disopred3
PrDOS
Aggrescan
Characterize charged amino acid cluster
Segmentation tool
- Sliding window technique
Sliding window technique
Score = number of charged amino acids / number of total amino acids in a window
Nst1
PE
F
Edc3
PE
APD
Nst1
PE
APD
G
Edc3
Edc3ΔPE
Edc3ΔAPD
4 h
24 h
H
Nst1
Nst1ΔPE
Nst1ΔAPD
4 h
24 h
I
Edc3
Edc3ΔPE
Edc3ΔAPD
Concentration(M)
J
Nst1
Nst1ΔPE
Nst1ΔAPD
Concentration(M)

927

Figure 1. ***Overexpression of Nst1 and Edc3 leads to mature condensate formation, whereas overexpression of their polyelectrolyte (PE) domain deletion mutants within the IDR maintains a stabilized microphase-separated state.***

(A) Schematic representation of budding yeast overexpression system to observe intracellular condensates.

(B) Diagram of puncta generation pattern of cells overexpressing GFP tagged Nst1 for 2 h (green) and 4 h (purple). *Δnst1* (YSK3490) cells transformed with pMW20-pGAL-GFP-NST1 were induced for 2 hours (green) and 4 hours (purple) under the GAL promoter. Cells were imaged and analyzed; mean integrated density and the number of puncta of each cell were measured and plotted.

(C-D) Representative fluorescence microscopy images and quantitative phase separation analysis of cells overexpressing GFP and GFP-tagged Nst1, Edc3, Dcp3, Dhh1, and Pab1. (C) Scale bar: 10 μm. (D) Cytoplasmic protein concentrations were measured via fluorescence correlation spectroscopy (FCS) as described in Materials and Methods. The puncta formation patterns in cells were classified into three categories: diffuse phase, microphase separation, and mature condensates. Box plot analysis of the correlation between the pattern of protein puncta formation and cytoplasmic concentration was presented.

(E) Schematic representation of polyelectrolyte (PE) domain segmentation.

(F) Sequence diagram of Nst1 and Edc3. The red box indicates the polyelectrolyte (PE) region, while the blue box represents the aggregation-prone domain (APD). Each sequence shown corresponds to the PE region. Positively charged amino acids, lysine (K) and arginine (R),, are highlighted in red and marked with a (+) sign below, whereas negatively charged amino acids, glutamic acid (E) and aspartic acid (D), are highlighted in blue and marked with a (–) sign below.

(G) Fluorescence microscopy images showing puncta formation in cells overexpressing Edc3 and each domain deletion mutant after 4 and 24 hours of galactose induction. In *Δedc3* cells (YSK3707), GFP-tagged full-length Edc3 (pMW20-pGAL-GFP-EDC3), Edc3ΔPE (pMW20-pGAL-GFP-EDC3ΔPE), and

Edc3 Δ APD (pMW20-pGAL-GFP-EDC3ΔAPD) were overexpressed. Representative images were selected from an average of more than 100 cells per strain at each time point. Scale bar: 5 µm.

(H) Fluorescence microscopy images showing puncta formation in cells expressing Nst1 and each Nst1 domain deletion mutant after 4 and 24 hours of induction as in (E). GFP-tagged full-length Nst1 (pMW20-pGAL-GFP-NST1), Nst1ΔPE (pMW20-pGAL-GFP-NST1ΔPE), and Nst1ΔAPD (pMW20-pGAL-GFP-NST1ΔAPD) were overexpressed in *Δnst1* (YSK3490) cells. Representative images were selected from an average of more than 100 cells per strain at each time point. Scale bar: 5 µm.

(I) Box plot analysis of the correlation between the puncta formation pattern and cytoplasmic concentration of the Edc3 and Edc3 derivatives. The puncta formation patterns in cells were classified into three categories: diffuse phase, microphase separation, and mature condensates. Cytoplasmic concentrations were measured in cells expressing each Edc3 domain deletion mutant after 4 hours of induction by fluorescence correlation spectroscopy (FCS) as described in Materials and Methods. The measured cytoplasmic concentrations of cells were analyzed with respect to puncta formation patterns.

(J) Box plot analysis of the correlation between the puncta formation pattern and cytoplasmic concentration of the Nst1 and Nst1 derivatives. The cytoplasmic protein concentration measurement and puncta formation analysis were performed same as (F).

Figure 2

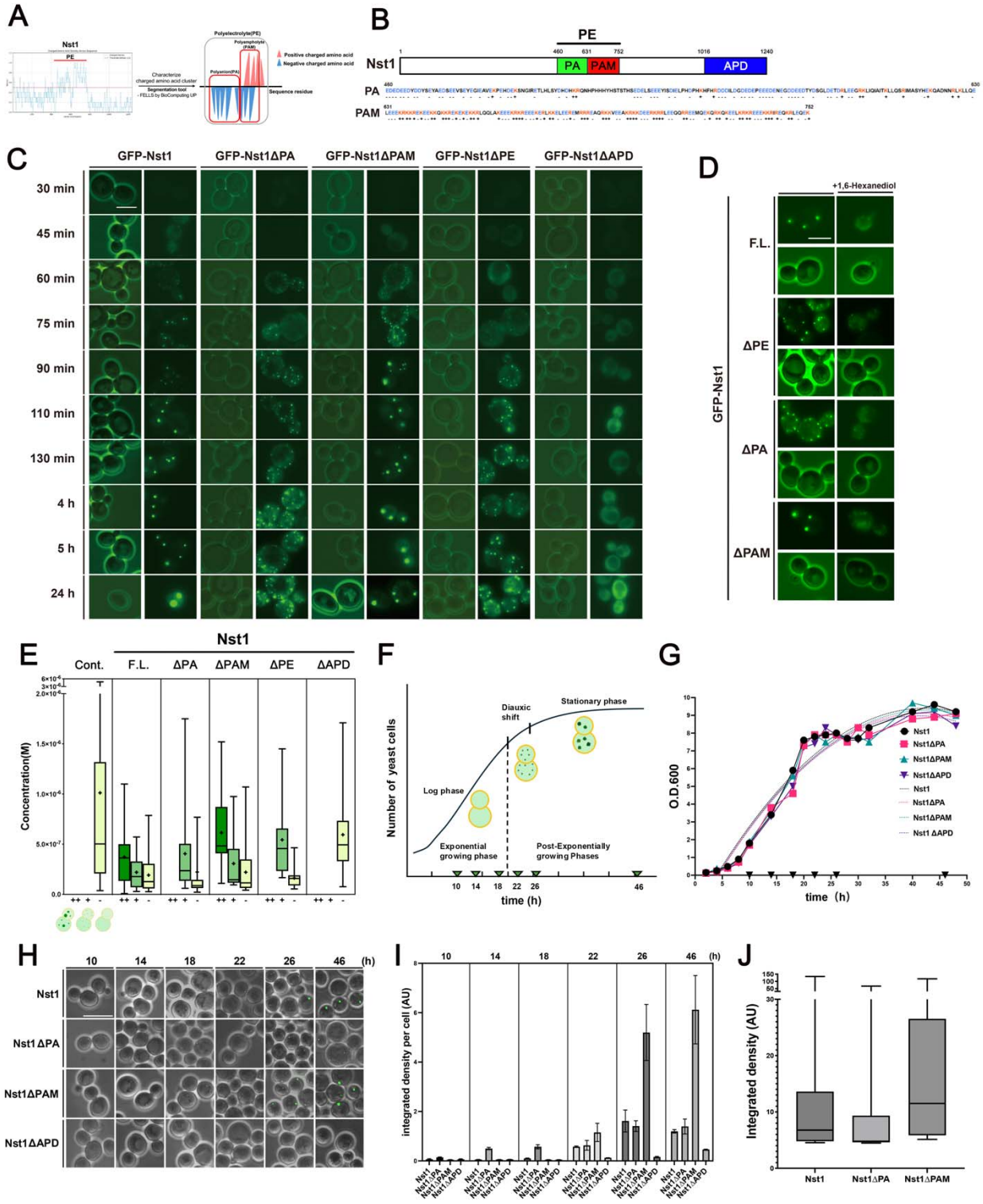
A
Nst1
PE
Characterize charged amino acid cluster
Segmentation tool
- FELLS by BioComputing UP
Polyelectrolyte(PE)
Polyampholyte (PAM)
Polyanion(PA)
Positive charged amino acid
Negative charged amino acid
Sequence residue
B
PE
Nst1
PA
PAM
APD
C
GFP-Nst1
GFP-Nst1ΔPA
GFP-Nst1ΔPAM
GFP-Nst1ΔPE
GFP-Nst1ΔAPD
30 min
45 min
60 min
75 min
90 min
110 min
130 min
4 h
5 h
24 h
D
+1,6-Hexanediol
GFP-Nst1
F.L.
ΔPE
ΔPA
ΔPAM
E
Nst1
Cont.
F.L.
ΔPA
ΔPAM
ΔPE
ΔAPD
Concentration(M)
F
Number of yeast cells
Diauxic shift
Stationary phase
Log phase
Exponential growing phase
Post-Exponentially growing Phases
time (h)
G
O.D.600
Nst1
Nst1ΔPA
Nst1ΔPAM
Nst1ΔAPD
Nst1
Nst1ΔPA
Nst1ΔPAM
Nst1 ΔAPD
time (h)
H
10
14
18
22
26
46
(h)
Nst1
Nst1ΔPA
Nst1ΔPAM
Nst1ΔAPD
I
integrated density per cell (AU)
J
Integrated density (AU)
Nst1
Nst1ΔPA
Nst1ΔPAM

970

Figure 2. ***Polyanion (PA) domain of the Polyelectrolyte (PE) region specifically promotes the coalescence of Nst1 condensates, whereas the polyampholyte (PAM) domain in the PE region does not.***

(A) Schematic representation of Polyanion (PA) and Polyampholyte (PAM) domain segmentation with a sliding window approach.

(B) Diagram of Nst1 with its domain architectures and sequences. The black line indicates the PE region, while the green, red, and blue boxes denote the PA, PAM, and APD regions, respectively. The amino acid sequences of the PA and PAM regions are shown below the diagram. Charges were annotated as described in Figure 1D.

(C) Fluorescence microscopy images of condensate formation in cells overexpressing each GFP-tagged Nst1 and its domain deletion mutants. Expression of GFP-tagged full-length Nst1 (pMW20-pGAL-GFP-NST1) or NST1 lacking specific domains - Nst1ΔPE (pMW20-pGAL-GFP-NST1ΔPE), Nst1ΔPA (pMW20-pGAL-GFP-NST1ΔPA), Nst1ΔPAM (pMW20-pGAL-GFP-NST1ΔPAM), and Nst1ΔAPD (pMW20-pGAL-GFP-NST1ΔAPD) - was induced in *Δnst1* (YSK3490) cells. Each domain deletion mutant was overexpressed by galactose induction for the indicated time periods. At each time point, fluorescence images were collected from at least 100 cells to ensure representativeness. Scale bar: 5 µm.

(D) Fluorescence microscopy images of GFP-tagged Nst1 condensates induced for 4 hours, followed by a 1-hour treatment with 1,6-hexanediol. Scale bar: 5 µm.

(E) Box plot analysis of the correlation between the puncta formation pattern and cytoplasmic concentration of cells overexpressing GFP-tagged Nst1, Nst1ΔPA, Nst1ΔPAM, Nst1ΔPE, and Nst1ΔAPD. Cytoplasmic protein concentrations were measured via fluorescence correlation spectroscopy (FCS). The puncta formation patterns in cells were classified into three categories: diffuse phase, microphase separation, and mature condensates.

(F-J) Biomolecular condensate formation of endogenously expressed GFP-tagged Nst1, Nst1ΔPA, Nst1ΔPAM and Nst1ΔAPD during chronological aging in yeast. (F) The growth phase diagram of general

budding yeast with observation time points designated. The inverted triangles (▾) on the x-axis represent the observed time points (10, 14, 18, 22, 26, and 46 hours). (G) Line chart showing the optical densities (O.D.600) of cell cultures endogenously expressing GFP-tagged Nst1, Nst1ΔPA, Nst1ΔPAM and Nst1ΔAPD under native NST1 promoter. The growth of *Δnst1* (YSK3490) cells integrated with pRS306-pNST1-GFP-NST1 full-length and various NST1 deletion mutants (YSK3700, YSK3701, YSK3702, YSK3714) was monitored over time. The 10 h,14 h and 18 h time points represent the log phase, 22 h the diauxic shift, and 26 h and 46 h the stationary phase. (H) Condensates were segmented using Fiji (ImageJ) and visualized in green. Shown are GFP images merged with corresponding phase-contrast images. Scale bar: 10 μm. (I) Bar plot showing the average integrated GFP fluorescence density per cell for each yeast strain expressing full-length Nst1 and its deletion mutants (Nst1ΔPA, Nst1ΔPAM, Nst1ΔAPD), as shown in (H). For each condition, more than 300 cells were analyzed using Fiji (ImageJ). Results are presented using GraphPad Prism 10. (J) Box plot showing the integrated GFP intensity of condensates in stationary-phase (46 h) yeast cells expressing Nst1, Nst1ΔPA and Nst1ΔPAM. For each condition, more than 300 cells were quantified using Fiji (ImageJ). Data from three independent biological replicates were plotted with GraphPad Prism 10.

Figure 3

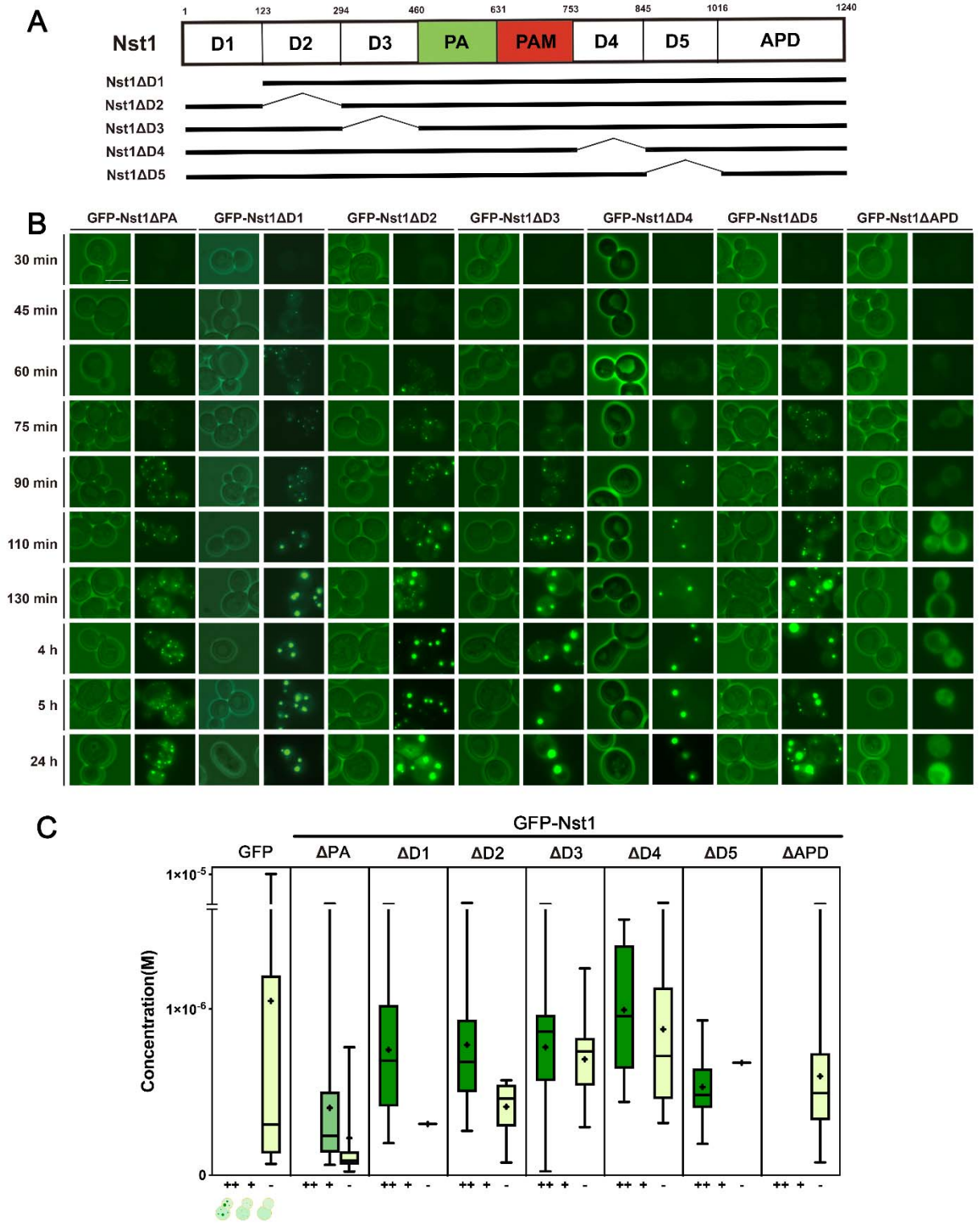

1012

1013

Figure 3. ***Polyanion (PA) domain exclusively functions in coalescence of Nst1 condensates.***

(A) A diagram of Nst1 with domain architectures. Residues 2-122 were designated as D1, 123-293 as D2, 294-459 as D3, 753-844 as D4, and 845-1015 as D5. The lengths of D1-D5 are similar to that of PA, and all of the domains are comparable in size.

(B) Representative fluorescence microscopy images comparing time-dependent condensate formation in the PA deletion mutant and other domain deletion mutants (ΔD1-D5, ΔAPD). In *Δnst1* (YSK3490) cells, GFP-tagged Nst1ΔPA (pMW20-pGAL-GFP-NST1ΔPA), Nst1ΔD1 (pMW20-pGAL-GFP-NST1ΔD1), Nst1ΔD2 (pMW20-pGAL-GFP-NST1ΔD2), Nst1ΔD3 (pMW20-pGAL-GFP-NST1ΔD3), Nst1ΔD4 (pMW20-pGAL-GFP-NST1ΔD4), Nst1ΔD5 (pMW20-pGAL-GFP-NST1ΔD5), and Nst1ΔAPD (pMW20-pGAL-GFP-NST1ΔAPD) were overexpressed. Overexpression of each Nst1 derivative was induced by galactose, and images were obtained at the designated time point after the induction. Representative images were selected among more than 100 cells. Scale bar: 5 µm.

(C) Box plot analysis showing the correlation between puncta formation patterns and cytoplasmic concentrations in the cells overexpressing GFP-tagged Nst1, Nst1ΔPA, NstΔD1-ΔD5, and Nst1ΔAPD after 4 hours of induction. Cytoplasmic protein concentrations were measured via fluorescence correlation spectroscopy (FCS). The puncta formation patterns in cells were classified into three categories: diffuse phase, microphase separation, and mature condensates.

Figure 4

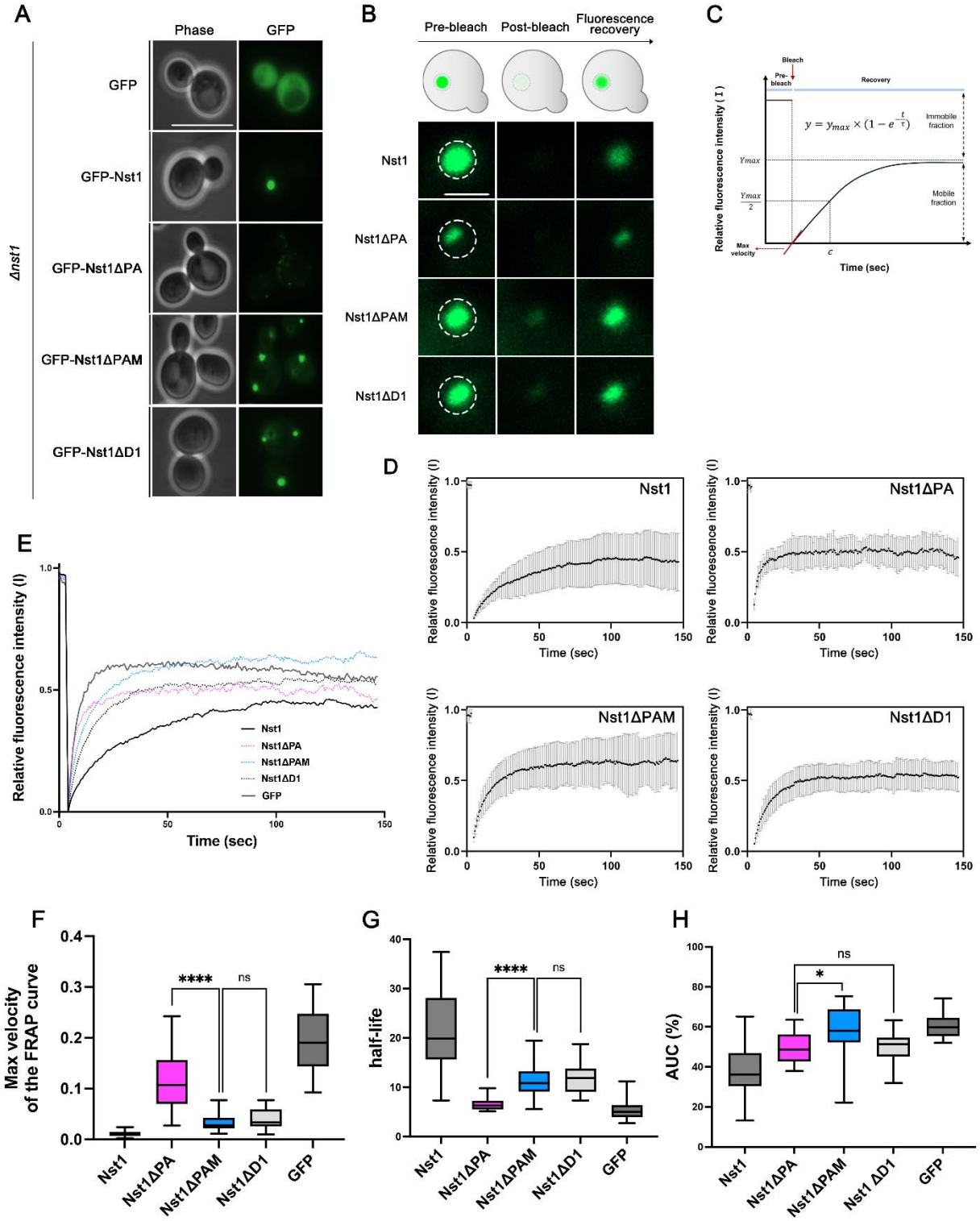

1033

Figure 4. ***The polyanion (PA) domain of Nst1 enhances intermolecular interaction, whereas the polyampholyte (PAM) domain increases the rigidity of Nst1 condensates.***

(A-H) GAL promoter induction was performed for *Δnst1* (YSK3490) cells transformed with pMW20-pGAL -GFP-NST1, pMW20-pGAL-GFP-NST1ΔPA, pMW20-pGAL-GFP-NST1ΔPAM, pMW20-pGAL-GFP-NST1ΔD1. Fluorescence Recovery After Photobleaching (FRAP) experiments were performed on induced condensates of these cells as described in Materials and Methods.

(A) Representative fluorescence microscopy images of cells overexpressing GFP-tagged full-length Nst1, Nst1ΔPA, Nst1ΔPAM, Nst1ΔD1, and GFP alone (control) in the *Δnst1* strain. Scale bar: 10 μm.

(B) Representative fluorescence microscopy images at pre-beach point (cycle 1 of 200), post-bleach (cycle 6 of 200), and fluorescence recovery (cycle 200 of 200) during FRAP analysis. The stitched lines indicate the region of interest (ROI) selected for bleaching the puncta in cells. All experiments were performed with more than 20 puncta each. Scale bar: 1 μm.

(C) Predicted FRAP recovery curve modeled as a single exponential function. t is time, y_{max} is the y value at infinite time ($t \approx \infty$), τ (tau) is the time point when the y value is equal to 63.2% of y_{max} value, and c is half-life.

(D) The average FRAP recovery curves of Nst1 and its mutants shown in (B). Each graph for full-length Nst1, Nst1ΔPA, Nst1ΔPAM, and Nst1ΔD1. The x-axis of these average graphs represents the time (sec) taken in 200 cycles, and the y-axis indicates the relative fluorescence intensity.

(E) The average FRAP recovery curves for Nst1 and all Nst1 mutants in (D) were plotted together for direct comparison. Full-length Nst1 (black line), Nst1ΔPA (pink dotted line), Nst1ΔPAM (blue dotted line), Nst1ΔD1 (black dotted line), and GFP (grey line) as a control. The x-axis and y-axis represent the same values as in (D).

(F) The maximum recovery rate of the FRAP curves for condensates of full-length Nst1, Nst1ΔPA, Nst1ΔPAM, and Nst1ΔD1. Akima spline interpolation was applied to all FRAP curves. For each Nst1 mutant, the first derivative (slope) at the point of maximal recovery rate was calculated using GraphPad

Prism 10. The y-axis represents the maximum recovery rate (maximum slope) of the fitted FRAP curve. Statistical significance was determined using unpaired two-tailed Student's t-test (**** $p<0.0001$) with Welch's correction. $P < 0.05$ was considered statistically significant.

(G) The half-lives of FRAP curves for condensates of full-length Nst1, Nst1ΔPA, Nst1ΔPAM, and Nst1ΔD1. The x-values corresponding to half-maximal recovery ($y = 0.5$) were calculated and averaged using GraphPad Prism 10. Statistical significance was determined using unpaired two-tailed Student's t-test (**** $p<0.0001$) with Welch's correction. $P < 0.05$ was considered statistically significant.

(H) The area under the curve (AUC) of the FRAP recovery curves for condensates of full-length Nst1, Nst1ΔPA, Nst1ΔPAM, and Nst1ΔD1. The AUC was calculated for each normalized FRAP recovery curve using GraphPad Prism 10. Statistical significance was determined using unpaired two-tailed Student's t-test (* $p<0.01$) with Welch's correction. $P < 0.05$ was considered statistically significant.

Figure 5

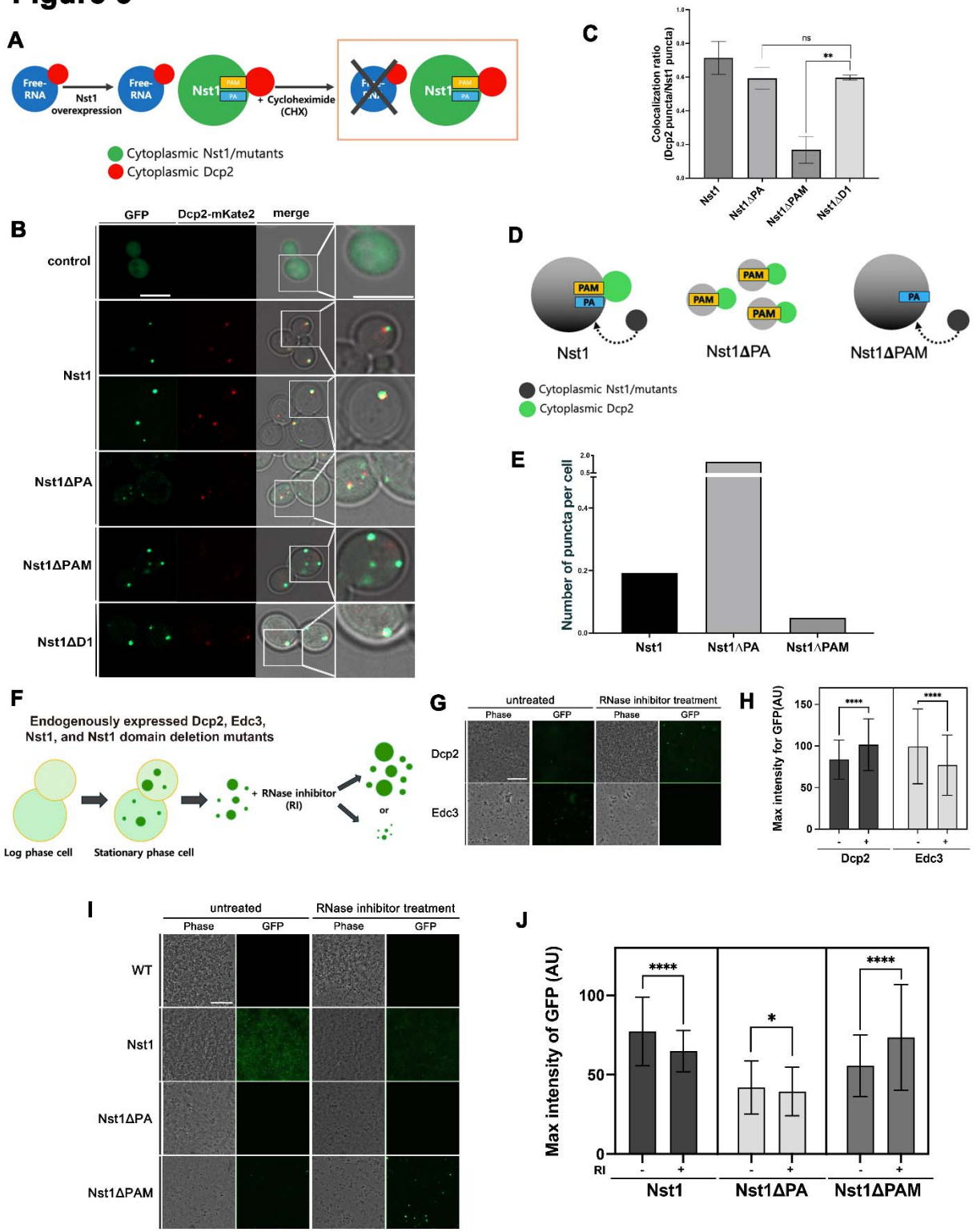

1072

Figure 5. ***The PAM domain is an RNA-independent multivalent interaction domain for interaction with the P-body component Dcp2.***

(A) Schematic representation of the experiments (B-C) designed to examine the effect of RNA on P-body condensate formation of Nst1 and its PA and PAM deletion mutants.

(B) High-resolution confocal microscopy images showing the formation of mKate2-tagged Dcp2 condensates induced by condensates of GFP-tagged Nst1, Nst1ΔPA, Nst1ΔPAM, and Nst1ΔD1. W303a *Δnst1* cells endogenously expressing Dcp2-mKate2 (YSK3663) were transformed with pMW20-pGAL-GFP-NST1, pMW20-pGAL-GFP-NST1ΔPA, pMW20-pGAL-GFP-NST1ΔPAM, or vector only (control). Following galactose induction for 4 hours, cells were treated with cycloheximide (CHX, 100 µg/ml) for 10 minutes and imaged using a Zeiss LSM 980 confocal microscope equipped with an Airyscan 2 detector (Carl Zeiss). The right panel shows a 2× magnified view of selected puncta in the merged images. GFP and mKate2 channels are shown in green and red, respectively. Scale bar: 5 µm. Representative images are shown.

(C) Quantitative analysis of the spatial co-localization between Dcp2 and Nst1 condensates shown in (B) after CHX-treatment. The co-localization ratio was calculated as the proportion of Dcp2 condensates overlapping with Nst1 and its mutants-derived puncta. Puncta were segmented and quantified using Fiji (ImageJ) software. For each Nst1 and its mutants, at least 100 condensates were analyzed per experiment across three independent replicates. Statistical significance was determined by unpaired t-test (***$p < 0.001$) using GraphPad Prism 10.

(D) Schematic representation of the proposed Dcp2 condensation model based on the functional roles of the PA and PAM domains of Nst1.

(E) Quantification of Dcp2-EGFP puncta formation in yeast cells (YSK3709) imaged by widefield epifluorescence microscopy. Cells endogenously expressing Dcp2-EGFP were transformed to overexpress Nst1, Nst1ΔPA, or Nst1ΔPAM for 4 hours. Images were acquired using identical microscope settings for all conditions. Dcp2-EGFP puncta were segmented in FIJI (ImageJ) by intensity thresholding.

The number of puncta per cell was quantified and normalized by cell number, with more than 300 cells analyzed for each condition. Data are presented as bar graphs generated using GraphPad Prism 10.

(F) Schematic illustration of the experimental workflow for the experiments (G–J) designed to elucidate the roles of the PA and PAM domains in condensate formation with respect to free-RNA.

(F-J) For endogenous-level expression, w303a, w303a expressing chromosomally EGFP-tagged Nst1, Dcp2, or Edc3, and *Δnst1* strains expressing chromosomally integrated GFP-Nst1ΔPA or GFP-Nst1ΔPAM were cultured for 30 hours. Cells were lysed with or without RNase inhibitor, and insoluble pellets were collected. All experiments were performed at least three times.

(G, I) Phase-contrast and fluorescence images of cell pellets prepared with or without RNase inhibitor. Condensates composed of GFP-tagged Dcp2 and Edc3 for (G), or Nst1, Nst1ΔPA, and Nst1ΔPAM for (I), were formed in stationary phase cells (30 hour cultured), collected, and visualized. Each experiment was repeated three times, with more than five images acquired per experiment. Scale bar: 10 μm.

(H, J) Quantification of the maximum intensity values of segmented puncta from the images in (G) was shown in (H), and from (J) is shown in (I). For each punctum, the maximum intensity was measured by segmenting puncta within the top 0.05% of intensity values using Fiji. Statistical significance was assessed by unpaired t-test (****$p < 0.0001$) using GraphPad Prism 10.

Figure 6

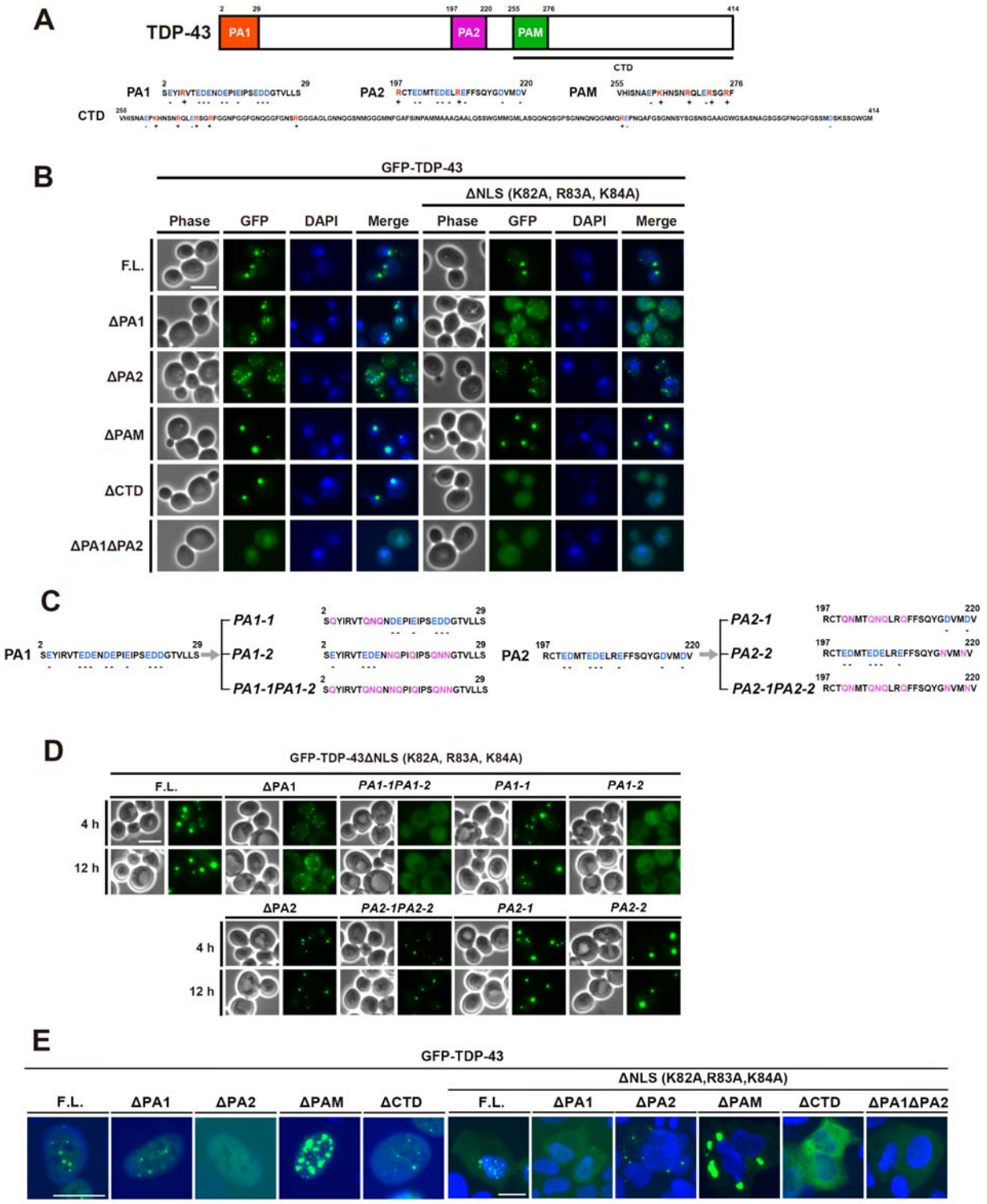

1117

Figure 6. ***The Polyanion (PA) domain of Edc3 and human TDP-43 promote coalescence of condensates, similar to Nst1.***

(A) Schematic representation of TDP-43 domain architecture. Residues 2–29 and 197–220 were identified as clusters of negatively charged amino acids, designated PA1 and PA2, based on a sliding window approach and prediction tools, as described in Supplementary Figure 3. The region spanning residue 255-276 was denoted as PAM, while residues 255-414 were characterized as the C-terminal domain. See also Supplementary figure 3.

(B) Representative widefield fluorescence microscopy images of budding yeast (W303a) cells after 4 hours of overexpression of TDP-43 and its domain deletion mutants (ΔPA1, ΔPA2, ΔPAM, ΔCTD and ΔPA1ΔPA2) with or without NLS (Nuclear localization signal) sequence under a galactose-inducible promoter. Cells were fixed and stained with DAPI to visualize nuclei. Scale bar: 5 µm.

(C) The amino acid sequence of the PA1 and PA2 domains of TDP-43, along with its *PA1-1, PA1-2, PA1-1PA1-2, PA2-1, PA2-2,* and *PA2-1PA2-2* mutant variants, is depicted at the top. In the *PA1-1, PA1-2, PA1-1PA1-2, PA2-1, PA2-2,* and *PA2-1PA2-2* mutants, the negatively charged glutamic acid (E) and aspartic acid (D) residues were individually substituted with glutamine (Q) and asparagine (N), respectively, as indicated.

(D) Representative widefield fluorescence microscopy images are shown for budding yeast (W303a) cells overexpressing TDP-43 full-length (F.L.), each PA domain deletion mutants (ΔPA1 and ΔPA2), as well as the *PA1-1PA1-2, PA1-1, PA1-2, PA2-1PA2-2, PA2-1*, and *PA2-2* variants, all of which lack the NLS. Images were taken following 4 and 12 hours of galactose induction. For each strain and time point, more than 100 cells were examined, and representative images are presented. Scale bar: 5 µm.

(E) Representative wildfield fluorescence microscopy images of cells expressing GFP-tagged TDP-43 and its variants (ΔPA1, ΔPA2, ΔPAM, ΔCTD and ΔPA1ΔPA2) in U2OS cells at 48 hours after transfection. U2OS cells were transfected with plasmids encoding GFP-tagged TDP-43 variants under

CMV promoter as described in Materials and Methods. After 48 hours, cells were observed using fluorescence microscopy to assess condensation pattern of each TDP-43 variant. Scale bar: 20 μm.